Effect of injection strategies on particulate matter structures of a turbocharged GDI engine

Marco Potenza, Marco Milanese, Arturo de Risi

University of Salento, Department of Engineering for Innovation, 73100 Lecce, Italy

Abstract

A study on particulate matter (PM) compound of a turbocharged gasoline direct injection (GDI) engine for different injection strategies has been performed. Particularly, morphology and structure of PM and soot produced by GDI engine were investigated as a function of injection rail pressure and start of injection before top dead center (SOI bTDC). The produced particulate matter and soot have been analyzed on a wide range of operating conditions by means of imaging and sampling techniques. To study the relationship between particulate morphology and engine working conditions, microscopic analyses (SEM and TEM) of several samples at the exhaust were performed. Therefore, these investigations were coupled with soot measurements before the catalyst and at the exhaust by means of a soot detector, able to measure the carbon component of particulate matter. Besides, the same measurements were compared with smoke opacity analyses to detect also the non-carbon components. The results demonstrated high influence of injection strategies on soot morphology-composition and on catalyst efficiency, revealing also a wear phenomenon of the piston under high pressure condition.

Keywords: soot morphology, particulate matter, emissions, injection strategies

1. Introduction

In the last decades, the interest of scientific community in pollutants production from automotive sector and their reduction has grown continuously because, as it is well known, engines are one of the main cause of gaseous and ultra-fine solid particles emissions. Compression ignition (CI) diesel engines are associated with relatively high particulate matter (PM) emissions that have been recognized as harmful for environment and dangerous for human health, being carcinogenic and causing respiratory diseases [1]-[3]. On the other hand, port fuel injection spark ignition (SI) gasoline engines are characterized by negligible soot (carbonaceous compounds) and PM emissions [4], but higher values of CO_2 that is one of the major causes of global warming [5]-[7]. In order to reduce CO_2 emissions of SI engines, new technologies have been developed and engine downsizing has been proposed as possible direction for pollutant reduction [8]-[10]. For this reason, gasoline direct injection (GDI) engines coupled with high

performance turbocharger systems have been developed in recent years [11]-[14]. In addition to CO_2 reduction, it has been demonstrated that vehicles powered by turbocharged downsized gasoline engines yield fuel savings up to 20% with respect to traditional SI engines moving vehicles of the same weight. However, GDI engines are characterized by higher soot production with respect to traditional SI and CI engines with particulates filter [15]: although the homogeneous stoichiometric premixed combustion is adopted in GDI engines, air-fuel mixing is not enough for complete fuel evaporation and local fuel-rich zones are formed into the combustion chamber with subsequent high soot formation [11],[16]. Furthermore, depending on injection strategies, such as high rail pressure with high penetration length or high injection angle with piston near to top dead center (TDC), fuel may impinge piston head or valves with subsequent pool fire combustion [17] and increment in soot production.

The soot-PM produced by turbocharged GDI engines is characterized by nano-scale dimension and is mainly produced during transitory, cold start and high engine speed regimes [15]. The PM emitted by internal combustion engines is mainly constituted by soot, ash, volatile organic and sulphur compounds from fuel and lube oil [16],[18]-[22] or metal compounds from engine wear and fuel [23], that have high toxicological influence on human health.

As GDI engines diffusion and installation on commercial light duty vehicles are quickly increasing, due to their low CO_2 emissions, the particulate emission reduction is the key point for current and future researches. A deep understanding of PM compound morphology, dimension, composition and concentration can help the development of new devices or particulate filters for emissions reduction. Furthermore, by knowing the influence of injection parameters on PM compound production and concentration, a reduction of pollutants can be achieved by modifying the engine control unit (ECU) parameters, that might results in a parallel increment in soot dimension up to micrometric size and a subsequent reduction of reactive sites [11],[24].

For a better understanding of PM morphology, diameters distribution, composition and concentration, SEM-TEM analyses are the most commonly used methods [25]-[33], coupled with selected area electron diffraction (SAED) [27], x-ray investigations (EDX-XRD) [27],[34],[35], thermogravimetric analysis (TGA) [36],[37], Raman spectroscopy [27],[38], exhaust sampling [18],[39],[40] or in chamber imaging for soot measurements on flame (Two Colour Method, Laser Induced Incandescence) [41]-[47]. As regards to microscopic study on soot morphology, previous researches focused on injection strategy variation (lean and rich conditions, high-load case and advance of ignition) [28], emissions produced during standard driving profiles (NEDC and WLTC) [11],[29],[48] or comparing the soot produced by gasoline engines with diesel soot in order to identify morphological differences and similarities [30] or

comparing soot characteristics produced using different fuels in spark ignition engines [49]-[52]. Some other researchers, dealing with electronic microscopy study of soot, investigated the influence of different fuels [25], [26], [53]-[54].

In the present work, based on electronic microscopic images (SEM-TEM) of soot particles sampled by copper grid specimens at the exhaust of a commercial turbocharged GDI engine, the PM compound morphology has been studied, by varying the injection parameters that could affect soot production. Since in addition to carbonate compound, metallic particles have been found on the copper grid, Energy Dispersive X-ray (EDX) analyses have been performed to deep investigate the PM composition. Finally, to correlate PM compound morphology and distribution with conventional exhaust sampling techniques, opacity (for PM quantity determination) and soot concentration have been measured at the engine exhaust and before the catalyst, thus obtaining the catalyst efficiency in soot/PM oxidation.

2. Experimental setup

In this work, several experiments were carried out on a 4-stroke 1.4 liters turbocharged GDI engine coupled with AVL DynoPerform 240 Eddy current dynamometer, driven by AVL CDC 400 controller, through AVL LSE 410 power unit. In Table 1 the main characteristics of the engine are reported.

Table 1. Characteristics of the GDI engine.

Engine type	Four stoke, GDI, 4 cylinders, turbocharged
Valves/Cylinder	4
Displacement (cm^3)	1390
Bore (mm)	76.5
Stroke (mm)	75.6
Compression ratio	10:1
Max power (kW@mm^{-1})	90@5000
Max torque (Nm@mm^{-1})	200@[1500-4000]
Catalyst	TWC

To monitor the engine parameters, such as in cylinder pressure, intake and exhaust temperature, engine oil and coolant temperature, 2 independent acquisition boards were used for high and low speed signals. The first one was a National Instruments NI PCI-6123 board, 8 channels, able to acquire up to 3.2

MS/s/channel, while the second one was a National Instruments compact DAQ cDAQ-9172 board coupled with a NI 9205 module, 32 channels, that can acquire up to 250 kS/s. Furthermore, by means of AVL 733S gravimetric fuel meters, the instantaneous (10 Hz acquisition rate frequency) and the average gasoline consumption were measured during the engine tests. Data consistency was checked by an online mass-balance implemented in the engine monitoring software.

The engine ECU parameters were monitored and modified by means of ETAS ES590 interface module via Ethernet. The interface was connected with the engine ECU by means of a K-line cable. In order to modify the ECU calibration, INCA software was used. Through ASAM interface and by means of ASAP3 protocol, the ECU PC controller was coupled with the engine monitoring PC by a RS232 connection. All engine parameters, fuel consumption and the main ECU parameters were monitored and acquired by a PC through a National Instrument LabView software developed for this purpose. In Figure 1 a scheme of the experimental setup is reported.
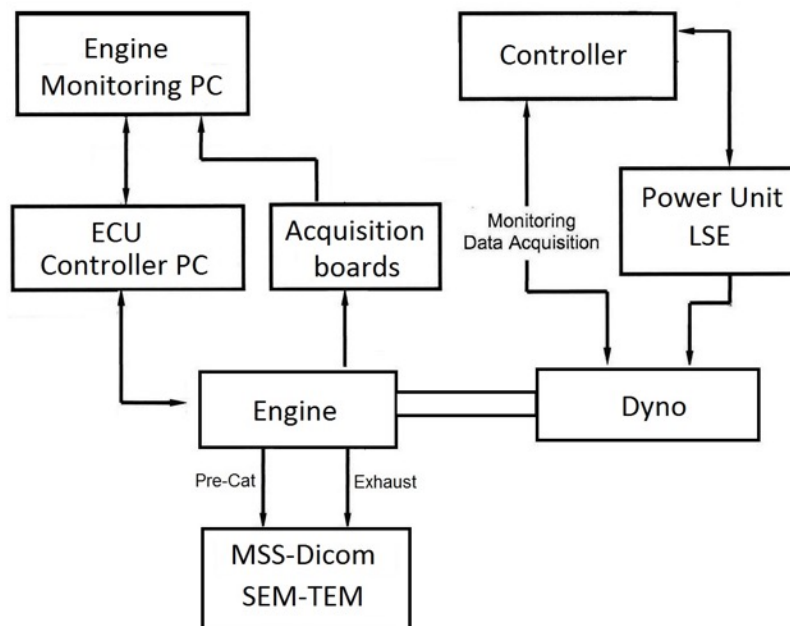

Figure 1. Scheme of the experimental setup.

In order to analyze the carbonate compounds morphology and concentrations, sampling and imaging techniques have been applied to the engine exhaust, before and after the catalyst. Furthermore, taking into account that soot/PM oxidation is highly temperature dependent, as oxidation rate becomes relevant above 600 °C [28],[55],[56], in order to investigate the catalyst efficiency, all tests in this work have been carried out, keeping the catalyst intake temperature at 726 ± 4 °C [22],[57]-[59].

Several SEM/TEM analyses have been executed on specimens (copper grids) taken at the exhaust via thermophoretic sampling techniques. The thermophoretic phenomenon is referred to the deposition of solid particles dispersed into a fluid, due to a temperature gradient between gas and specimen surface [60]-[62]. Copper grids with 300 meshes and 3 mm diameter were used as PM deposition surfaces for SEM analyses, while TEM analyses required different grids with carbon coating on the specimen. All grids were cooled at about 7 °C, in order to increase the temperature gradient, allowing a better PM deposition on the specimen. Finally, thermophoretic sampling was performed at constant engine speed of 1000 rpm and 50 Nm of load for 1 second.

The SEM analyses were executed by means of ZEISS EVO 40 high vacuum microscope that allowed to work up to 1:1000000 of magnification ratio, being its maximum resolution equal to 4 nm at 30 kV, depending on specimen characteristics and images contrast.

The Transmissions Electronic Microscope LEO 922 operating with an electron acceleration voltage of 200 kV, 0.29 nm resolution was used to execute TEM, SAED and EDX analyses.

In order to correlate PM composition with conventional sampling techniques at the exhaust, a comparison between 2 sampling techniques has been performed in the last part of the present work. Particularly, the Micro Soot Sensor (MSS) AVL-MSS and the opacimeter AVL DICOM 4000 have been applied. The first one, whose working principle is based on the photo-acoustic effect (a pulsed IR laser producing periodic heating around soot particles, generates a pressure pulse, directly proportional to the mass concentration of carbon black [63] (soot particles are strongly absorbing the MSS laser pulses, despite other solid particles, whose acoustic effect is therefore negligible), which is acquired by a high sensitivity microphone placed into a resonant chamber) was used to measure the soot concentration (carbon fraction of particulate matter). While, the opacimeter AVL DICOM 4000 was used to measure the total PM concentration. The working principle of this instrument is based on the light absorption effect due to solid particles dispersed into a fluid. By considering a light beam with intensity I_0 propagating into a fluid in thermal equilibrium with an optical path length L, the light extinction can be expressed according to the Lambert-Beer law [64]:

$$I(L) = I_0 e^{-\sigma L} \tag{1}$$

where σ, the particle cross section related to the extinction coefficient, can be expressed as follows:

$$\sigma = \int_0^\infty N(r) Q_{ext}(\lambda, m, r) \pi r^2 dr \tag{2}$$

According to Mie theory [65],[66], in Eq. 2, $N(r)$ is the number of particles having radius r, $m = n - ik$ is the complex refraction index of particles and $Q_{ext}(\lambda, m, r)$ is the extinction efficiency for spherical

particles with known optical properties. Therefore, the extinction through a medium is composed by 2 contributes:

$$Q_{ext} = Q_{abs} + Q_{scat} \tag{3}$$

where Q_{scat} is the scattering efficiency for spherical particles and Q_{abs} is the absorption efficiency. The measured intensity by the sensor, I, depends on particles radius and composition as well as laser source wavelength. This means that all the opaque particles (carbon, oil lubricant/HC, fuel/HC, metallic) produce light absorption unlike as in a photo-acoustic sensor (e.g. AVL MSS) able to detect only the carbon component of particulate matter.

2.1. Measurement points identification

Since the aim of the present work was the study of PM compound produced by a turbocharged GDI engine, different injection strategies (modification of ECU values as start of injection crank angle and rail pressure) have been tested at engine speed of 1000 rpm and load of 50 Nm, in order to identify crucial sooting conditions of low speed vehicles, starting without turbocharger functioning. Particularly, once reached the engine operating point of 1000 rpm 50 Nm and set the rail pressure to 50 bar, a scheduled increment of rail pressure was performed, starting from 50 up to 120 bar with steps of 10 bar. After the last set point was reached, the rail pressure was reset to 50 bar and a new scan with several start of injection crank angles (up to 340 CA° bTDC with increment steps of 10 CA°) was tested. For each ECU point, several analyses have been realized, according to the summary in Table 2.

Table 2. List of measurement points and analyses.

ID	ECU parameters		SEM	TEM/SAED	EDX	Soot concentration	Opacity
	SOI (CA°)	Rail pressure (bar)					
1	270	50	☑	☑	☑	☑	☑
2	270	60	☐	☐	☐	☑	☑
3	270	70	☐	☐	☐	☑	☑
4	270	80	☑	☑	☑	☑	☑
5	270	90	☐	☐	☐	☑	☑
6	270	100	☐	☐	☐	☑	☑
7	270	110	☐	☐	☐	☑	☑
8	270	120	☑	☑	☐	☑	☑
9	280	50	☐	☐	☐	☑	☑
10	290	50	☐	☐	☐	☑	☑
11	300	50	☑	☑	☐	☑	☑
12	310	50	☐	☐	☐	☑	☑
13	320	50	☐	☐	☐	☑	☑
14	330	50	☐	☐	☐	☑	☑
15	340	50	☑	☑	☐	☑	☑

The fuel consumption, measured by a fuel balance, was almost constant (1.89 ± 0.09 kg/h) during all tests confirming that the different injection strategies did not affect the total fuel consumption significantly.

3. Results and discussion

3.1. SEM, TEM, SAED and EDX analysis

In this section, the results of several SEM, TEM, SAED and EDX analyses are presented. The SEM analyses allowed to study morphology and dimension of soot and PM particles, while higher resolution TEM images coupled with SAED and EDX analyses were used to study in depth their morphology/composition.

In Figure 2, two SEM images at different magnifications, related to the test case 1, at 50 bar rail pressure and 270 CA° bTDC SOI, are reported.
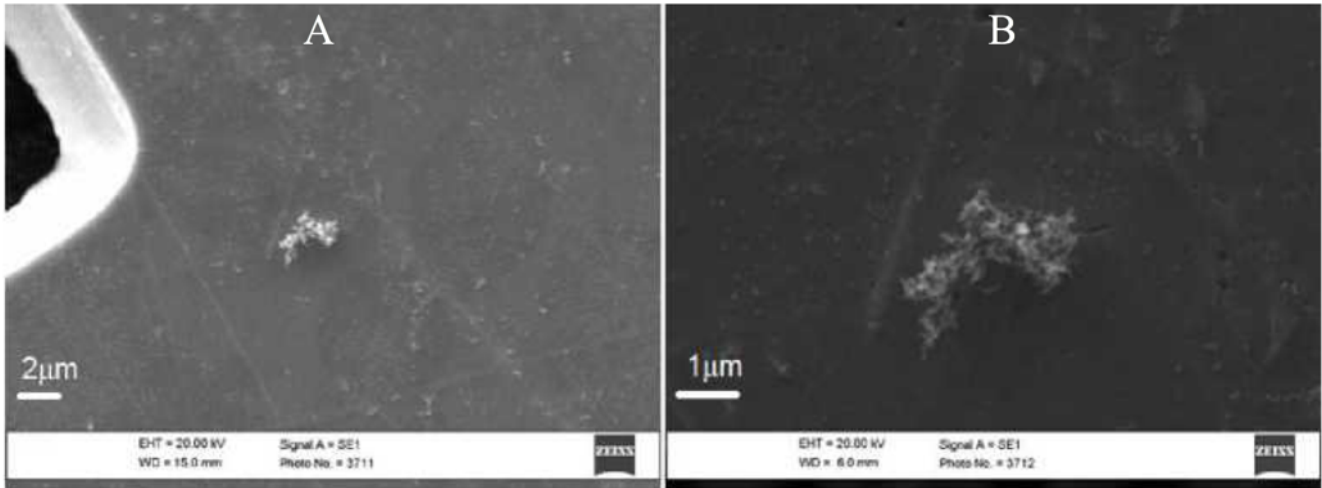
Figure 2. Test case 1; SEM images at different magnifications (A: 3320 magnification; B: 10000 magnification).

As shown in Figure 2-A, no significant particulate deposition is detectable on the specimen at low magnification), while the higher magnification image (Figure 2-B) shows rare filament-like particles, having the main dimension of about 2 μm and several branched structures with lower dimension of about 200-500 nm: these particles are usually generated in high temperature well-premixed combustion processes. Under these conditions, soot particles coalesce in form of chain, due to the pressure of charged radicals in the flame: as the flame extinguishes, the free charges disappear and the chains coalesce without a preferential direction resulting in the larger agglomerates shown in Figure 2-B.
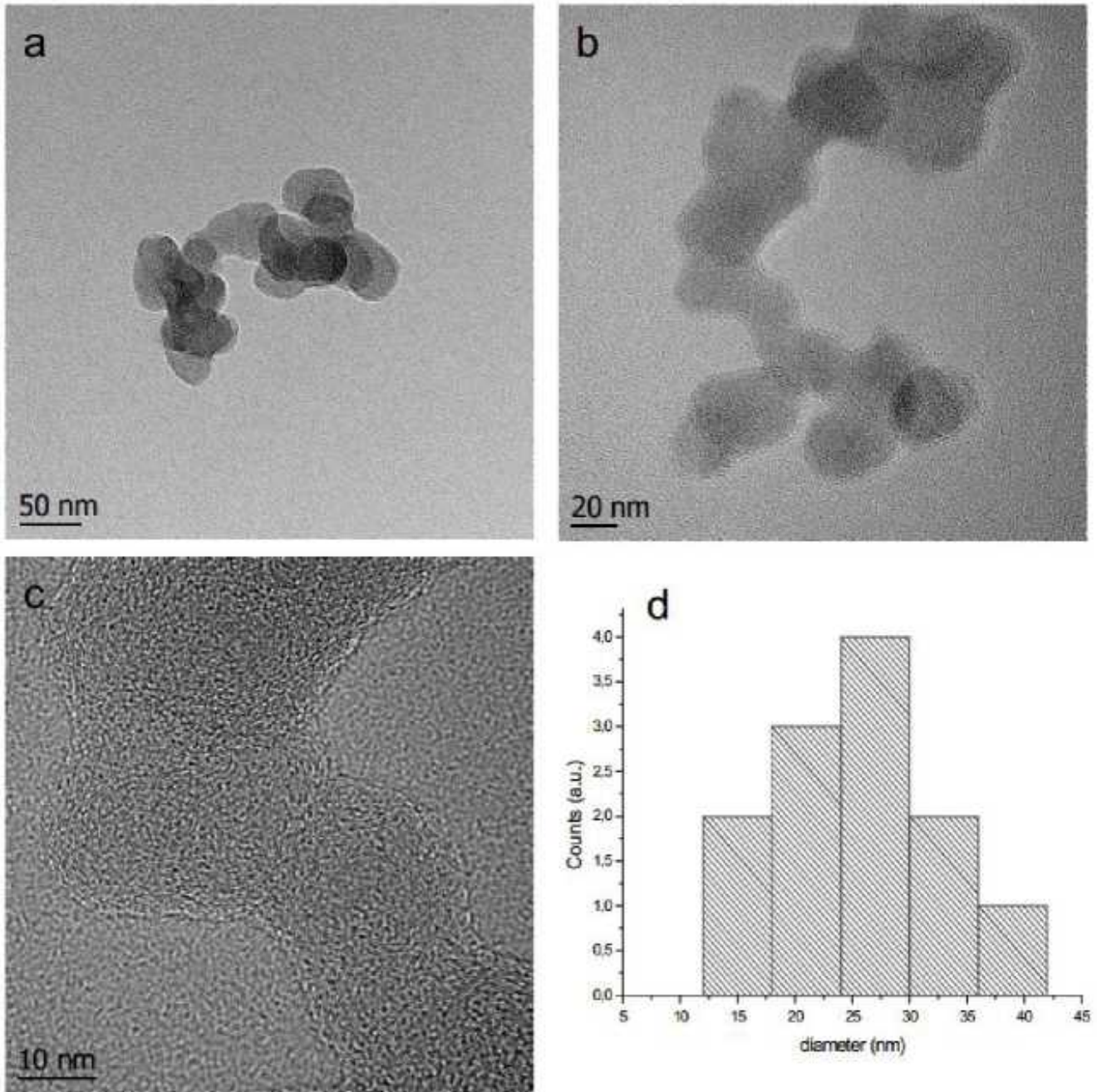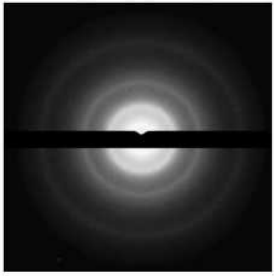
Figure 3. Test case 1; TEM images of graphite clustered nanoparticles at different magnifications (a, b and c) and mean diameters distribution (d), measured by Euclidean Distance Mapping (EDM) on the thresholded TEM images.

This assumption is confirmed by the TEM bright field images, reported in Figure 3, which show a typical carbon cluster with main dimension of about 260 nm and it is also strengthen through diffractometry (SAED analysis), in which crystal lattice structures of the particles have been analyzed by means of

Miller's indexes values (hkl): indeed according to [67], the diffraction image of particle produces a series of concentric circles, whose diameters represent the lattice main dimension into an orthogonal direction to the electron beam. Therefore, by knowing the main lattice dimension of the species, it is possible to analyze chemical composition of each particle. The results are summarized in Table 3.

Table 3. Test case 1; SAED analysis: nanoparticles diffraction image, experimental diffraction diameters and indexed diffraction diameters of carbon black [27].

	Experimental diameter (A)	Carbon indexed diameter (A)	hkl value
	D_1= 3.31	D_1 = 3.37	002
	D_2= 2.18	D_2 = 2.13	100
	D_3= 1.90	D_3 = 1.80	102
	D_4= 1.20	D_4 = 1.21	111

Experimental diffraction pattern of PM is similar to carbon black, having comparable diameters of the rings. Therefore, these results demonstrated that, in the first test case, a significant part of the clusters was composed by aggregates of carbon spheres with mean diameter of about 25 ± 7nm (see distribution reported in Figure 3-d measured by Euclidean Distance Mapping (EDM) on the thresholded TEM images [68]).
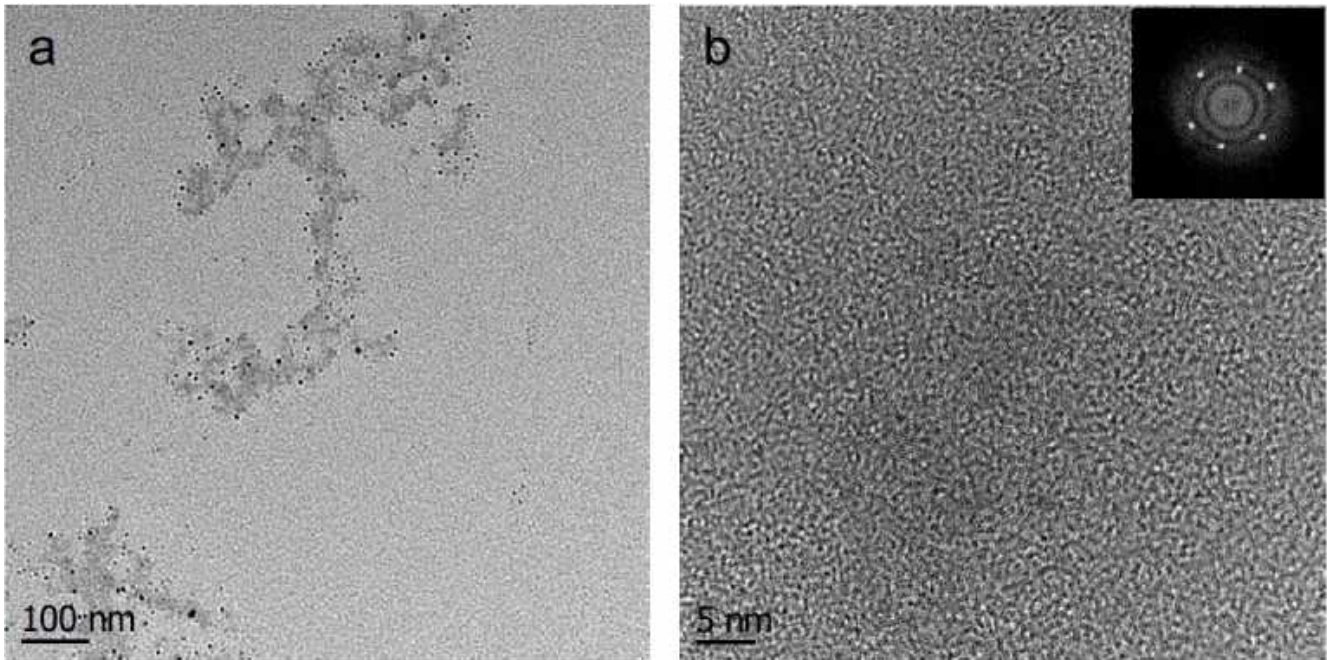
Figure 4. Test case 1: TEM images of metallic nanoparticles at different magnifications. A diffraction image is reported as the insert in b).

In addition to the above-discussed soot particles, in the test case 1, several polycrystalline aggregates have been also found on the specimen. They consisted of metallic nano-crystals with mean dimension of few nanometres (4 ± 1 nm) aggregated in cluster of about 500-700 nm, as it is evident in the high-resolution image of Figure 4-b.

To deepen the metallic nano-particles composition, an EDX analysis has been performed. The EDX spectrum, reported in Figure 5, shows traces of Cu and Si atoms in the nanoparticles; furthermore, as their inter-planar distances, ranged between 2 and 3 A (these values have been yielded according to [69] and [57], by the six high intensity spots detected in the diffraction image of Figure 4-b), it is possible to conclude that they are bonded into an alloy, while the formation of pure metallic crystals of Cu and Si can be ruled out. This experimental result is compatible with the piston material (40 - $AlSi_{12}Cu_3Ni_2Mg$), but not whit the combustion chamber alloy (aluminum and zirconium oxides) or with the lube oil (standard 5W20 composed mainly by Na, Ca, Zn, and P [20]). Finally, Chlorine traces are also present probably due to additives into fuel.
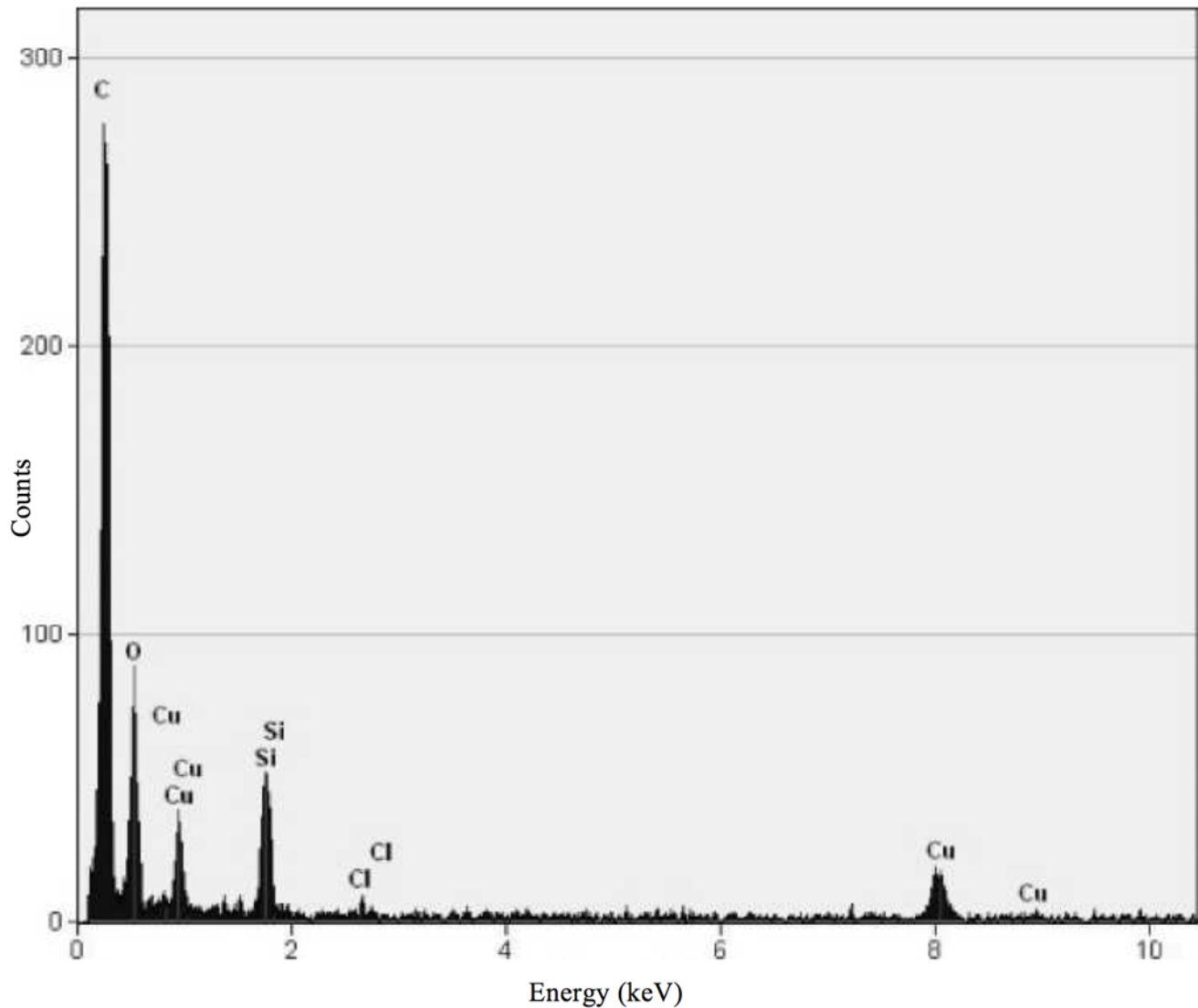
Figure 5. Test case 1: Metallic nanoparticles EDX spectrum.

The increment in rail pressure up to 80 bar (test case 4) leaded to higher particulate matter deposition, with respect to the 50 bar rail pressure case; furthermore, bigger particles with mean diameter up to 20 μm were also detected, as it is shown in Figure 6-A, where a plerosphere structure from coal fly ash is observable [58]. Besides, at higher SEM magnification, well-defined cloudy structures with filament-like particles can be seen around the big PM particle (Figure 6-B). Therefore, their morphology/composition has been investigated by means of TEM, SAED and EDX analysis.
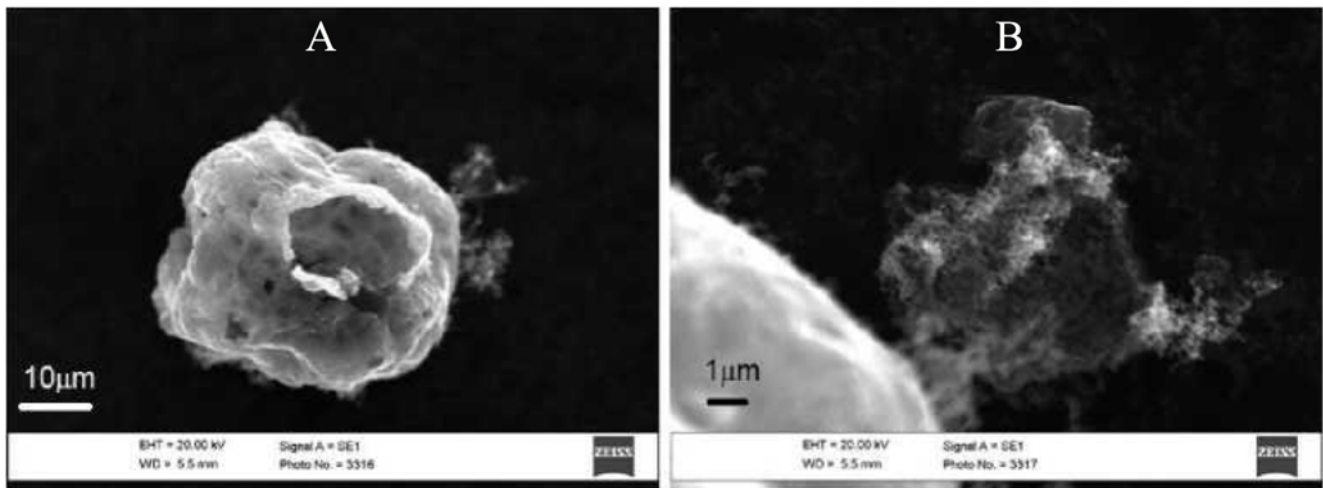
Figure 6. Test case 4: SEM images at different magnifications (A: 2300 magnification; B: 6500 magnification).

In the TEM bright field images of Figure 7 (a, b and c), typical carbon particles are shown; their composition is confirmed by the particle diffraction pattern reported in Table 4. In this case, the spheres, forming branched-like carbon clusters, have mean diameter of 38 ± 7 nm with the distribution of Figure 7-d, while the clusters are characterized by mean dimension of about 2 µm (Figure 7-a).
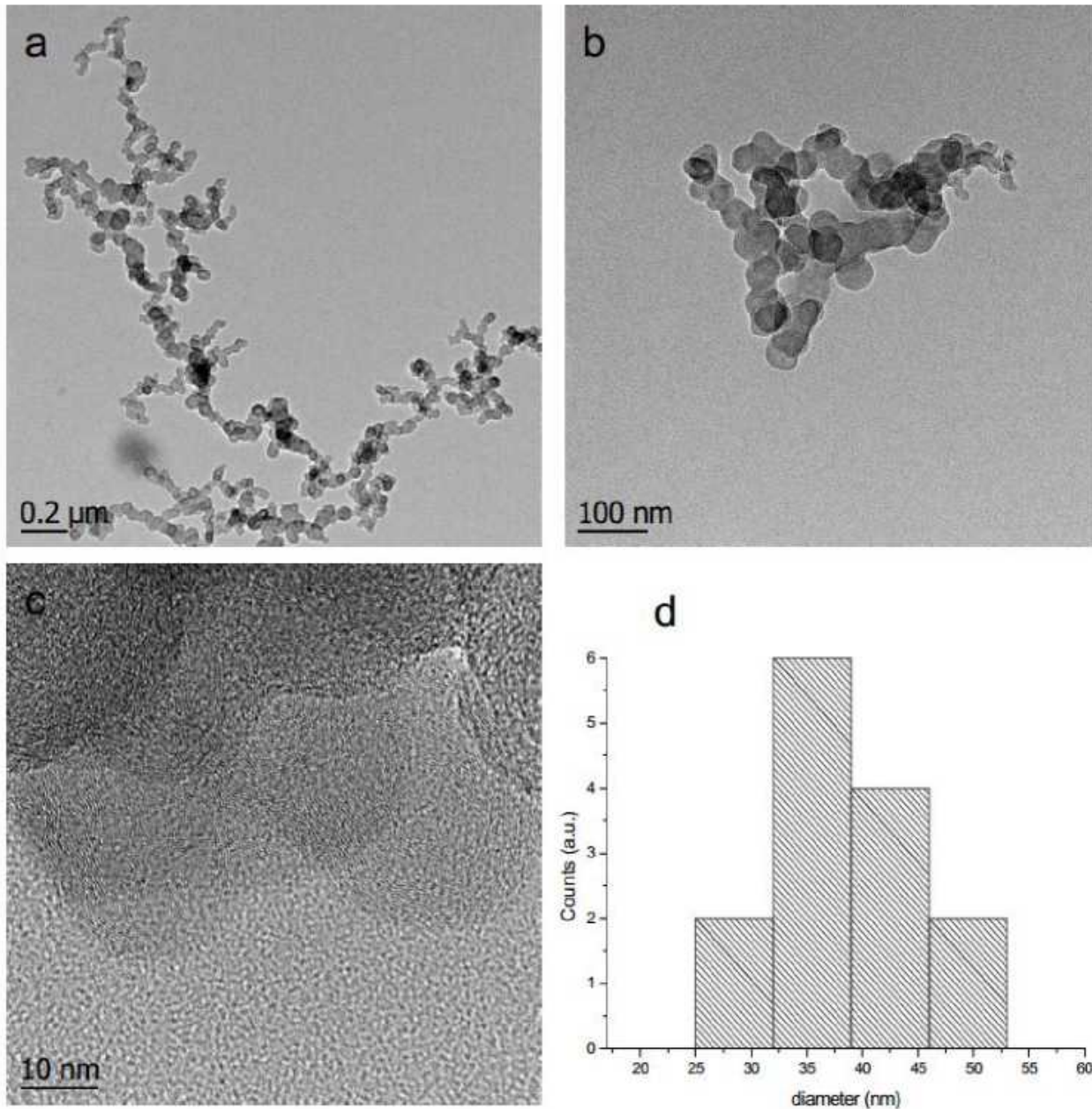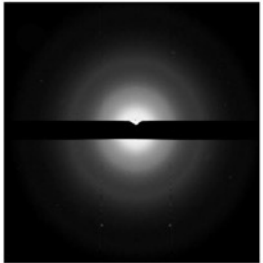
Figure 7. Test case 4: TEM images of graphite clustered nanoparticles at different magnifications (a, b and c) and mean diameters distribution (d), measured by Euclidean Distance Mapping (EDM) on the thresholded TEM images.

Table 4. Test case 4: SAED analysis: nanoparticles diffraction image and experimental diffraction diameters.

	Experimental diameter (A)
	$D_1 = 3.40$
	$D_2 = 2.10$
	$D_3 = 1.81$
	$D_4 = 1.25$

In the 80 bar 270 CA° bTDC injection conditions (test case 4), as also detected in the previous test case 1, several polycrystalline clusters have been found on the copper grid (see Figure 8), but unlike the previous point, this kind of particles have a higher number of nano-crystals and higher mean dimension $(6 \pm 1$ nm$)$.
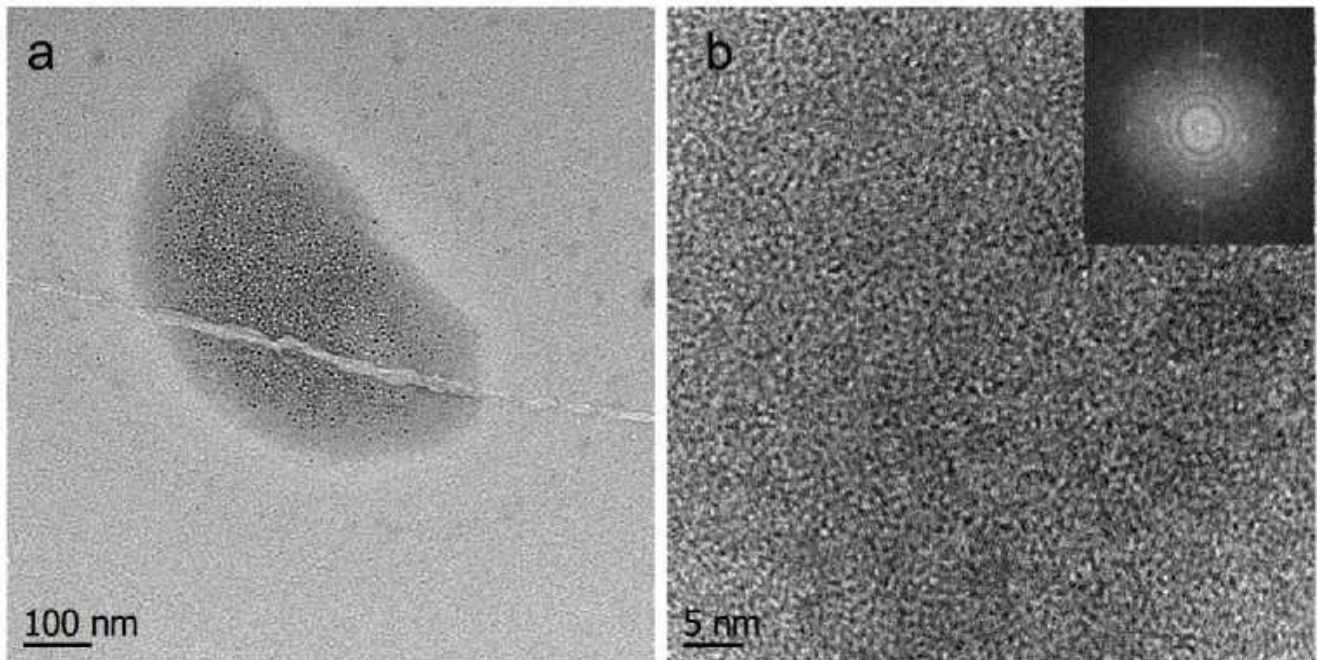
Figure 8. Test case 4: TEM images of metallic nanoparticles at different magnifications

Although, the diffraction image inserted in Figure 8-b shows a higher number of intensity spots with respect to the test case 1, also in this instance, the measured inter-planar distances resulted in the range of $2 - 3$ A, confirming the previous result. Besides, the EDX spectrum of metallic nanoparticles in Figure 9 shows Cu and Si peaks, compatible with the piston material, but unlike the previous case, these peaks

are more numerous and more intense, suggesting the presence of a growing piston wear phenomenon (the higher the counts, the higher the particles concentration in the specimen which are removed from the piston). Finally, Sulphur traces were founded on the specimen, probably related to fuel.
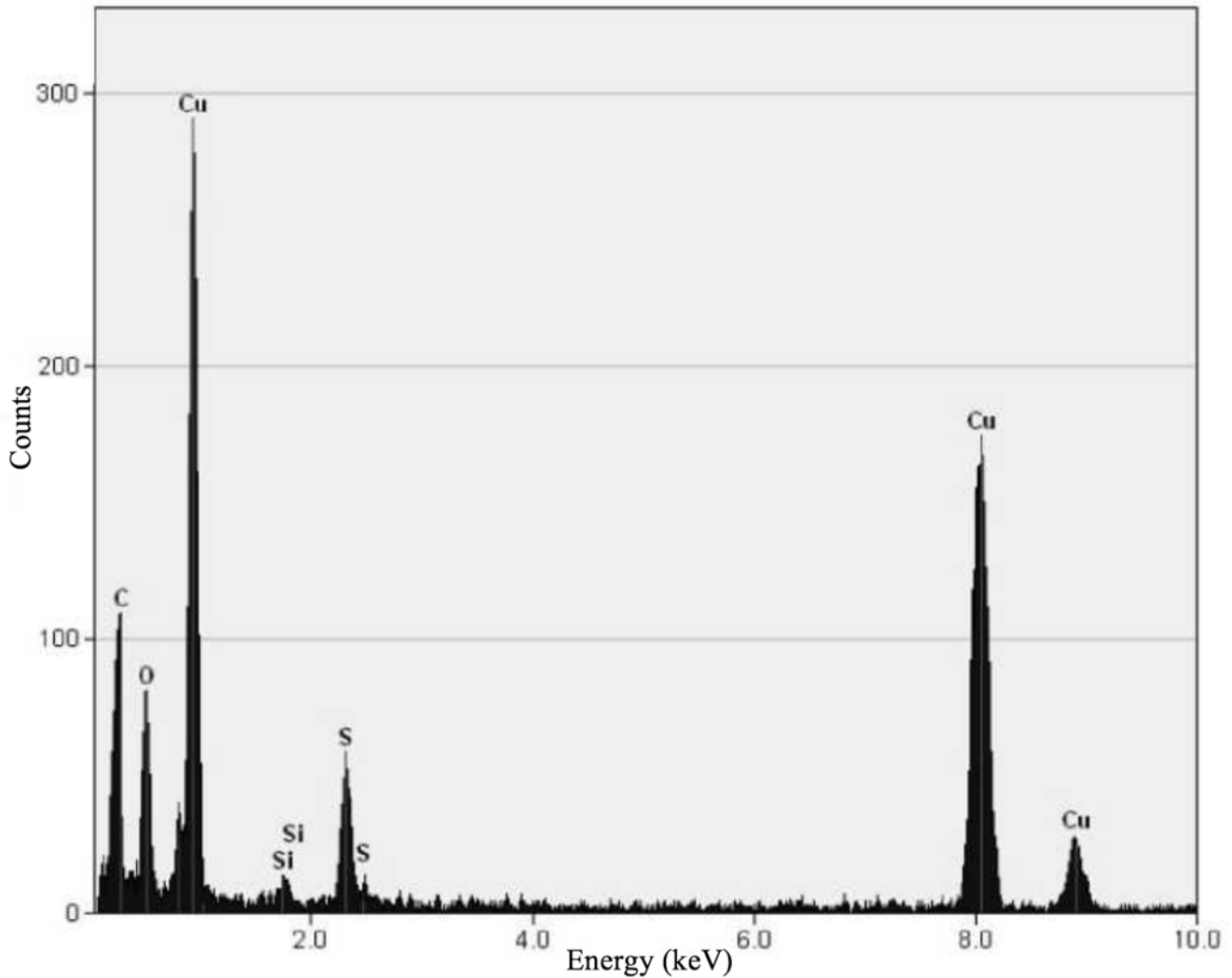
Figure 9. Test case 4: Metallic nanoparticles EDX spectrum.

In conclusion, the 80 bar, 270 CA° bTDC operative point (test case 4) was characterized by the production of carbonaceous and polycrystalline clusters, having higher dimensions with respect to the test case 1.

By further increasing of the rail pressure up to 120 bar (test case 8), more particles on the copper grid were observed; besides, the higher rail pressure influenced their dimension reducing them below the value of 2 μm (Figure 10-A). Also in this case, filament-like particles seem attached on bigger PM

particles, but unlike the previous pressure set points (50 and 80 bar), at 120 bar rail pressure several stand-alone not aggregated filament-like particles have been observed (Figure 10-B).
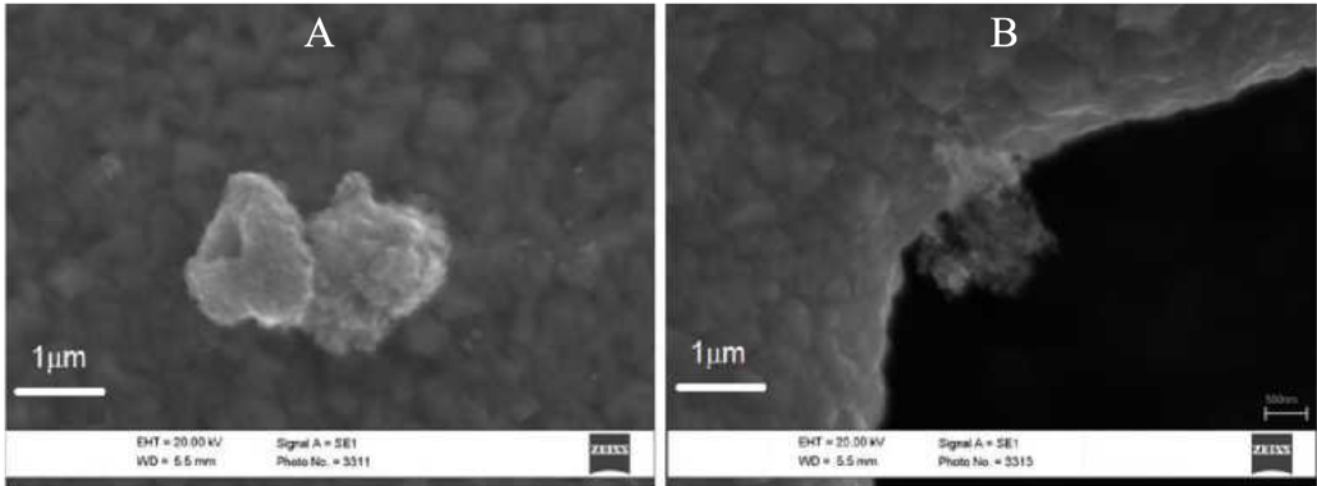

Figure 10. Test case 8: SEM images of two different particles at 15000 magnifications. In background the copper specimen can be observed.

The TEM analysis (Figure 11) showed 2 main different structures, despite the test cases at 50 and 80 bar:

- Crystal lattice nanoparticles of non-carbon metallic particulate matter, characterized by bimodal distribution of diameters, with small particles of 9 ± 4 nm and bigger particles of 27 ± 10 nm, uniformly distributed on the copper grid.
- Graphite structures with different morphology, aggregated into micro structures:
    1. one dimension structures nano-belt kind with core-shell morphology;
    2. nanotube structures;
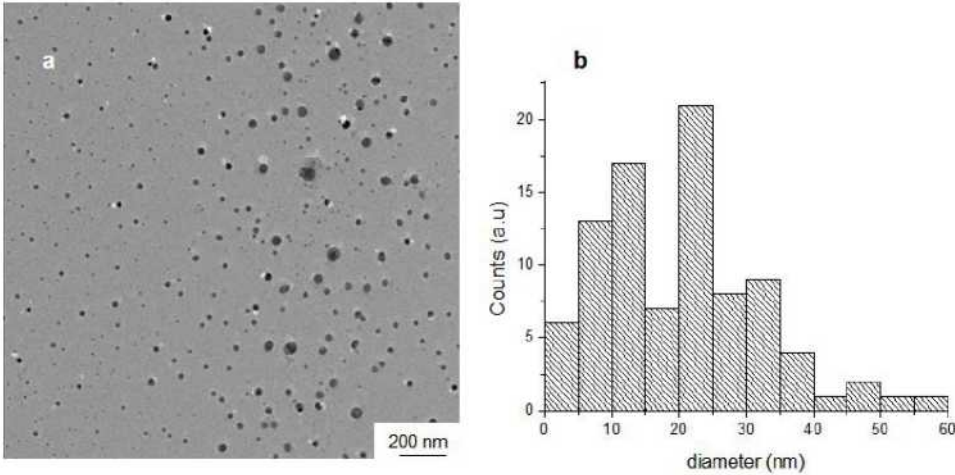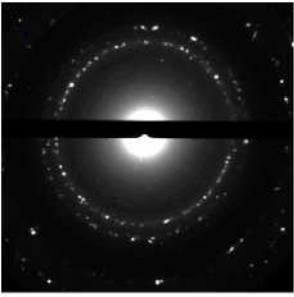   3. textured nano-foils structures.

Figure 11. Test case 8: TEM images of nanoparticles (a), diameters bimodal distribution (b), measured by Euclidean Distance Mapping (EDM) on the thresholded TEM images.

The diffraction image of the nanoparticles (reported in Table 5) is similar to a polycrystalline material, as can be deduced from the reticular distances. Indeed, some circles values cannot be associated to carbon particles, but to metallic oxides, such as aluminum or copper. Besides, the presence of several white spots on diffraction circles reveal the high variability of the material constituting the particles.

Table 5. Test case 8; SAED analysis: nanoparticles diffraction image and experimental and indexed diffraction diameters.

	Exp. diameter (A)	Indexed diameter (A)	hkl value
	$D_1 = 5.40$	5.43 (Si)	100
	$D_2 = 3.59$	3.54 (Cu)	100
	$D_3 = 3.45$	3.37 (C)	002
	$D_4 = 2.89$	2.89 (Cr)	110
	$D_5 = 2.77$	2.82 (Al)	220
	$D_6 = 2.60$	2.66 (Zn)	100
	$D_7 = 2.11$	2.13 (C)	100
	$D_8 = 1.83$	1.80 (C)	102
	$D_9 = 1.23$	1.21 (C)	111
	$D_{10} = 1.08$	1.04 (C)	20 (l=0)

By considering the interpretation of the data in Table 5, it can be assumed that, due to the high injection

pressure of 120 bar, piston abrasion occurred in relevant manner: the metallic compounds particles, in fact, are compatible with the piston material. In conclusion, the 120 bar and 270 CA° bTDC operative point seems to be very heavy in terms of piston abrasion, as confirmed by the high number of metallic particles found at the exhaust.

On the same specimen, together with metallic-compound nanoparticles, carbonaceous structures have been identified. In Figure 12 typical nano-belt graphite particles are shown, while their diffraction image and lattice dimensions are reported in Table 6. These structures have a typical core-shell morphology with a crystalline core (as evident from the typical bend contours) and an amorphous shell.
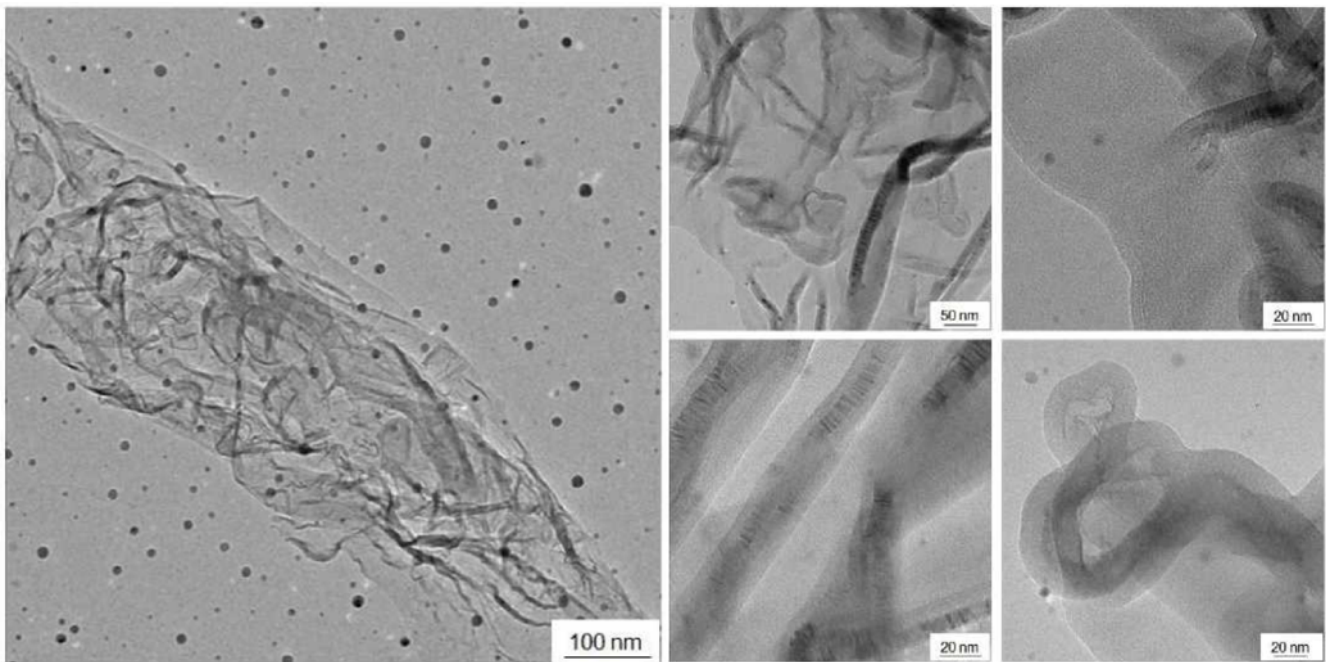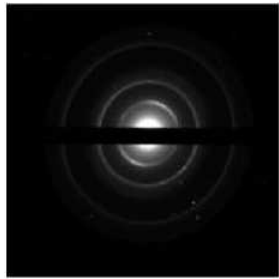

Figure 12. Test case 8: TEM images of nano-belt graphite structures with core-shell morphology

Table 6. Test case 8; SAED analysis: nano-belt particles diffraction image and experimental diffraction diameters.

	Experimental diameter (A)
	D_1= 3.40
	D_2= 2.13
	D_3= 1.76
	D_4= 1.19

Other typical structures found on the copper grid at 120 bar - 270 CA° bTDC operative point were nanotube-like particles, as reported in Figure 13.
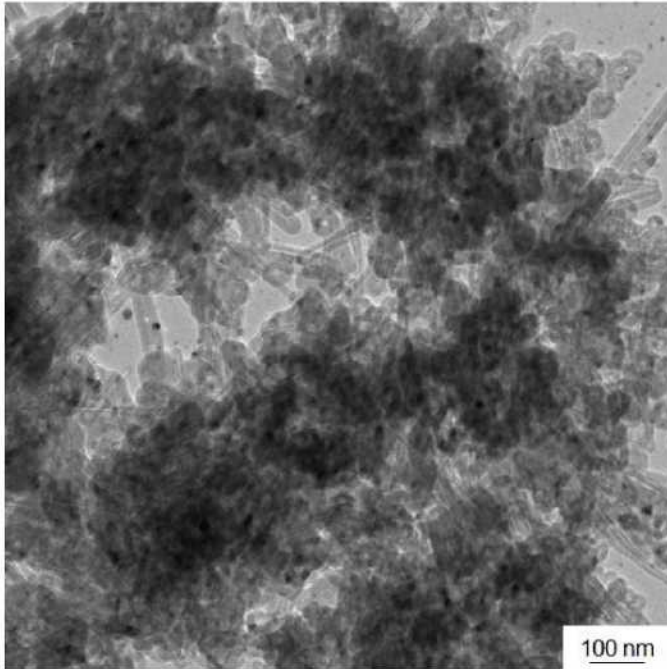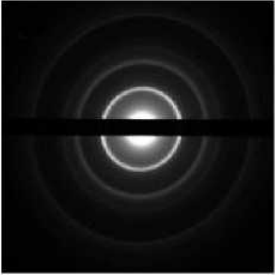
Figure 13. Test case 8: TEM images of nano-onion graphite structures

These particles are similar to those already observed by SEM analysis (Figure 10), presenting a filament-like morphology. Their mean diameter is about 20 nm. The planar lattice distances obtained from the diffraction image (Table 7) are in agreement with the carbon lattice in a graphite phase.

Table 7. Test case 8; SAED analysis: nano-onion particles diffraction image and experimental diffraction diameters.

	Experimental diameter (A)
	D_1= 3.40
	D_2= 2.13
	D_3= 1.76
	D_4= 1.19

The third carbon structures observed on the copper specimen were nanofoils textured particles (see

Figure 14). These structures were composed by different graphite carbon layers, with a hexagonal lattice structure and a regular alignment of the hexagons edge. The textured nature of these structures has been deduced from the diffraction image in Table 8, in which discontinuous rings with maximum of intensity along specific angular directions (white lines in figure) can be observed. In this case, the preferred orientation of the nanofoils was read by the lack of the main diffraction ring of the (002) lattice plane at 3.4 A. This lack indicates that the structure was oriented along the hexagon axis c perpendicular to the plane of the sample and the crystal growth occurred into a perpendicular direction to the specimen. The first Miller index in this configuration was equal to zero for each reticular plane. The bright field image of Figure 14 shows interfering Moire fringes due to the overlap of the (100) and (200) lattice layers.
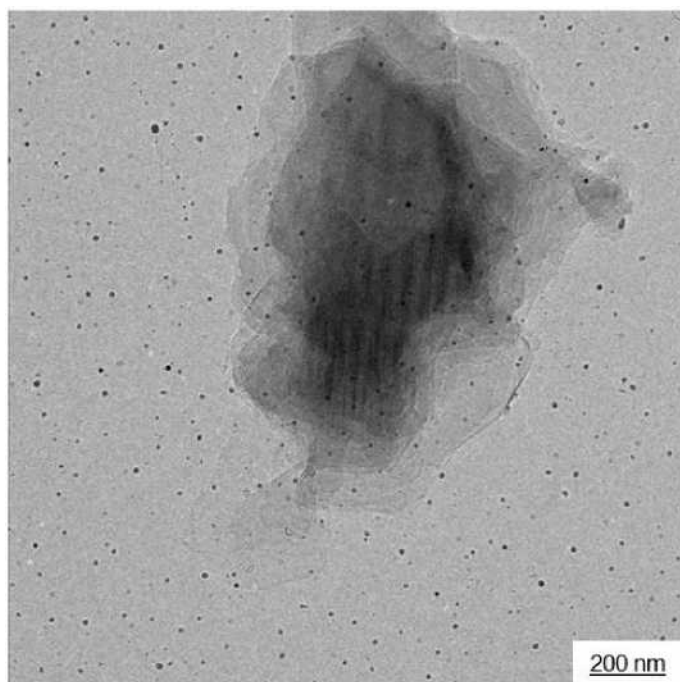

Figure 14. Test case 8: TEM images of nanofoils graphite structures

Table 8. Test case 8; SAED analysis: nanofoils particles diffraction image and experimental and indexed diffraction diameters

	Exp. diameter (A)	Indexed (A) carbon	hk (l=0)
	$D_1 = 2.13$	2.13	10
	$D_2 = 1.13$	1.23	11
	$D_3 = 1.04$	1.06	20
	$D_4 = 0.82$	0.81	12

In order to analyze in depth the relationship between ECU parameters and particulate morphology, the rail pressure was set to 50 bar, and 2 more SOI CAs were tested (test cases 11 and 15 in Table 2). Two SEM images at different magnifications of the copper grids at the exhaust for the test case 11 are reported in Figure 15.
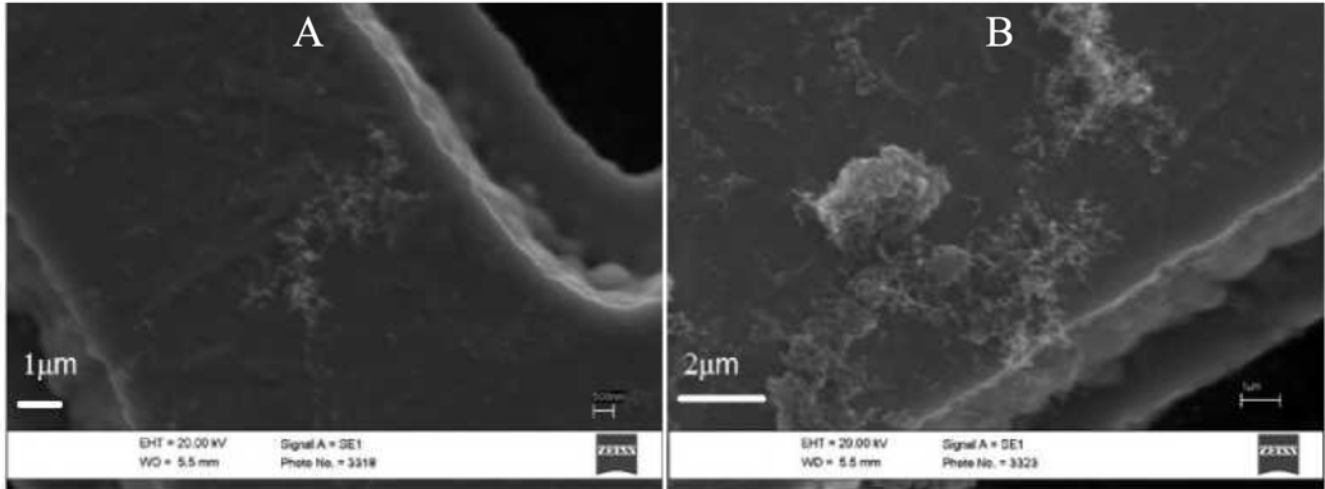

Figure 15. Test case 11: SEM images of two different particles at 7000 magnifications. In background the copper specimen can be observed.

At 7000 magnifications, it can be observed a high number of small filament-like aggregates of about 5 μm, with branched organization and well-defined small filament aggregations. Furthermore, in Figure 15-B, a sample of higher dimension PM particle of about 2 μm can be detected whit other small linear particles attached on the grid surface, which can be assumed to be carbon particles, as confirmed by the next TEM/SAED analysis.

In Figure 16 (a-b-c) several particles detected on the copper grid are shown for different magnifications. In this case, the main particles dimension is 28 ± 5nm with a mono-modal distribution as reported in Figure 16-d. A main cluster dimension between 100-350 nm has been measured on the specimen. The diffraction image in Table 9 demonstrates that the observed particles are carbon particles. Particularly, their structure seems a typical soot structure with carbon spheres aggregated together to form branched microparticles.

Finally, unlike the 50 bar 270 CA° bTDC, no significant concentration of metallic compounds and metal nanocrystals have been detected.

Figure 16. Test case 11: TEM images of graphite clustered nanoparticles at different magnifications (a,b and c) and mean diameters distribution (d), measured by Euclidean Distance Mapping (EDM) on the thresholded TEM images.

Table 9. Test case 11; SAED analysis: nanoparticles diffraction image and experimental diffraction diameters

	Experimental diameter (A)
	D_1= 3.36
	D_2= 2.21
	D_3= 1.75
	D_4= 1.27

In the last test case 15, a SOI of 340 CA° bTDC leaded to an increment in particulate matter dimension up to 20 μm, covered with filaments and aggregates of filaments: in Figure 17, in addition to a big PM particle, a uniform deposition of filament structures characterized by low dimensions (about 500 nm length) can be observed.
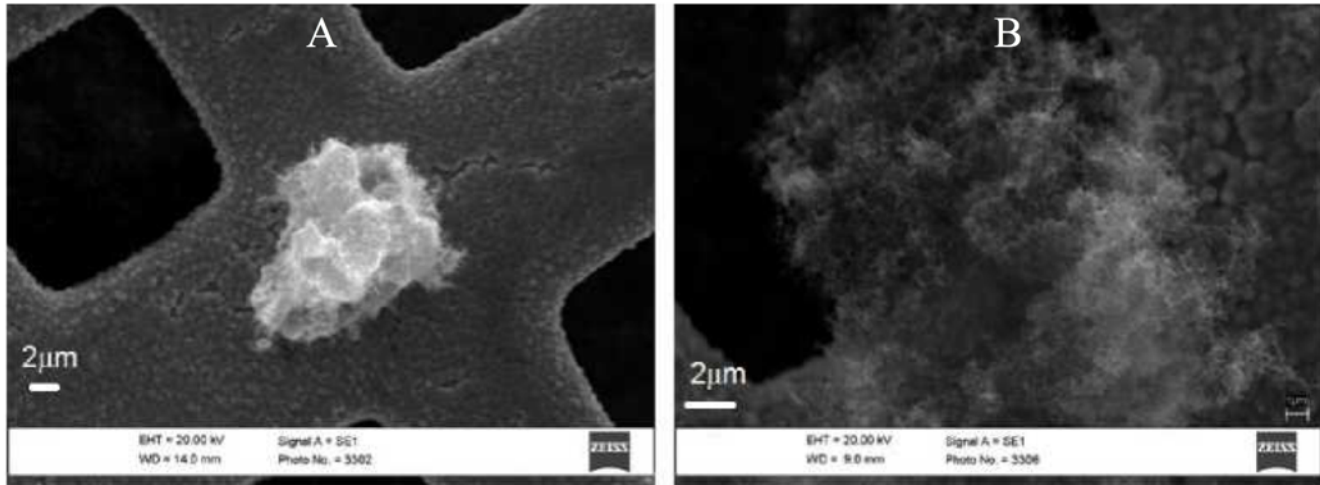
Figure 17. Test case 15: SEM images of two different particles at 4000 magnifications.

From the TEM analysis on the specimen, in this last operative point, only low dimension filament-like structures were found having main dimension of about 500nm (Figure 18).
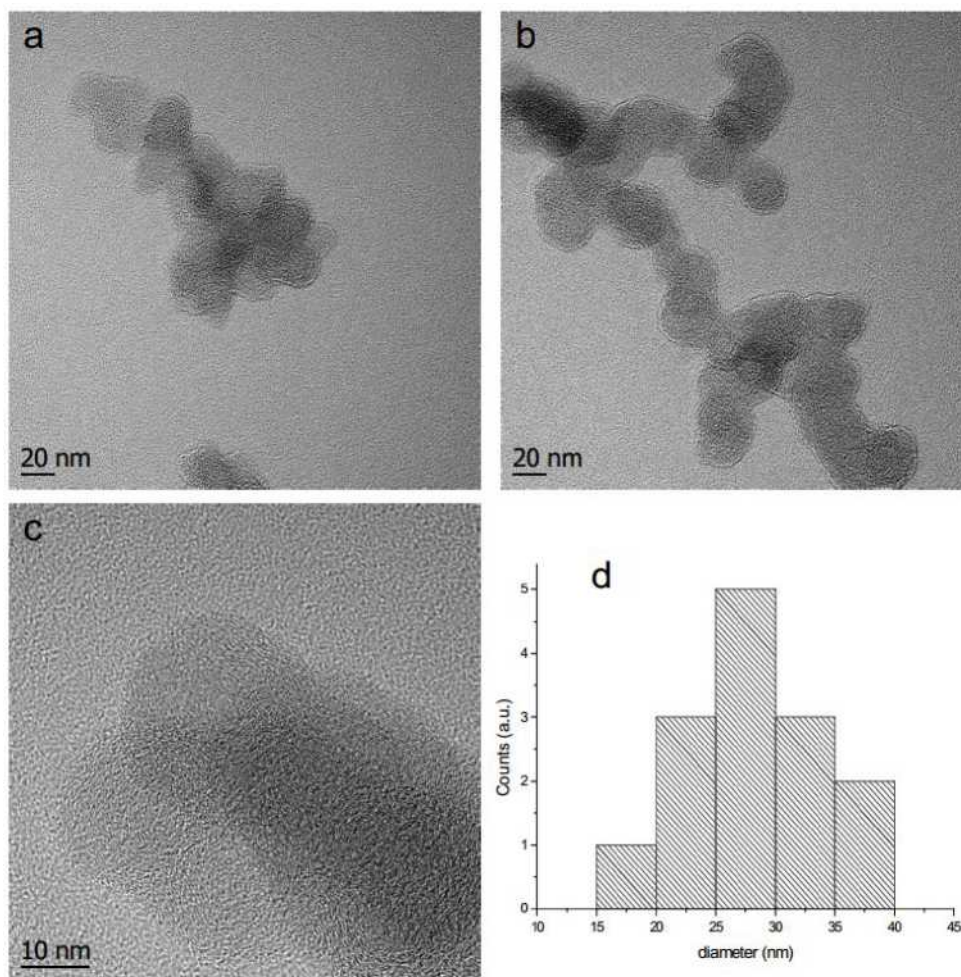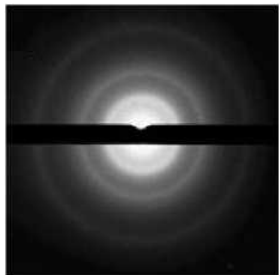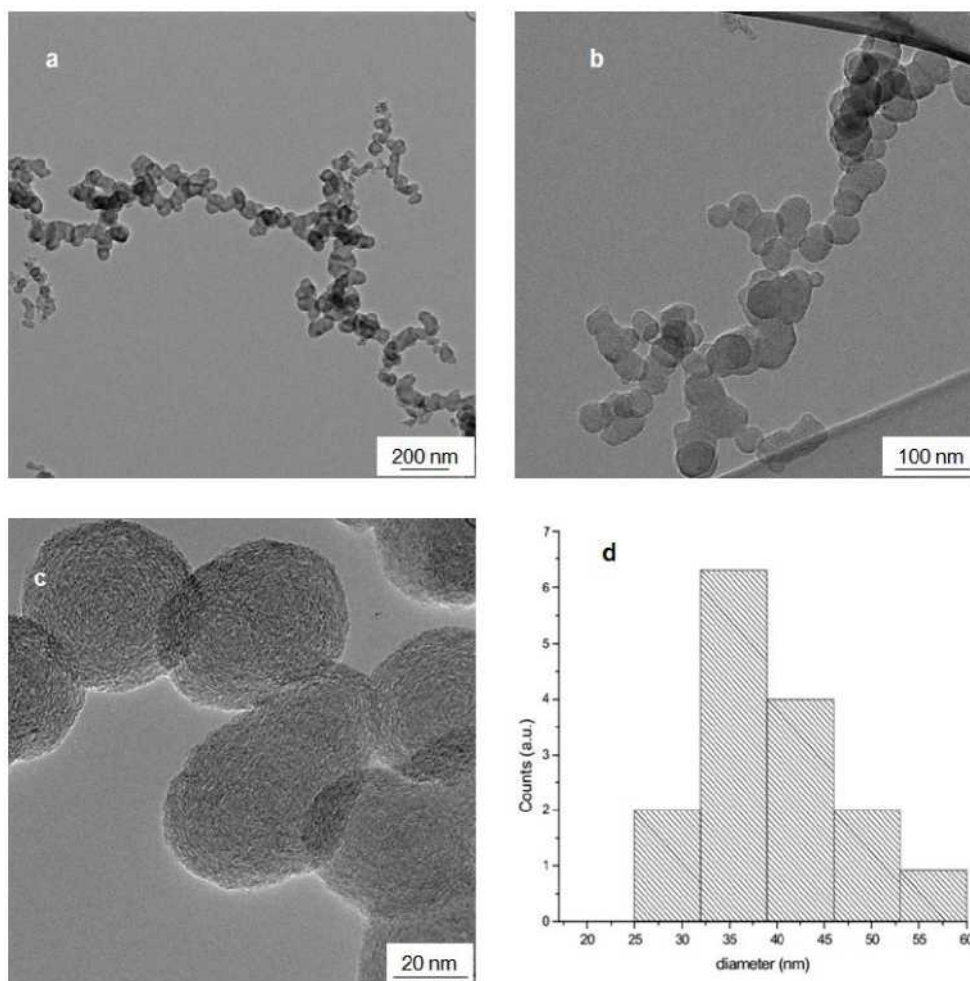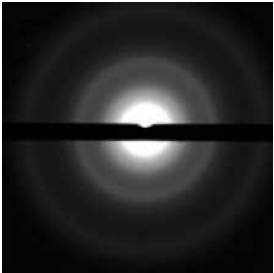
Figure 18. Teste case 15: TEM images of Graphite clustered nanoparticles at different magnifications (a,b ad c) and mean diameters distribution (d), measured by Euclidean Distance Mapping (EDM) on the thresholded TEM images.

These particles are uniformly distributed on the copper grid and have a mean diameter of 43 ± 12 nm (Figure 18-d). Their structure is a typical soot structure, composed by carbon spheres aggregated in a random branched mode with linear dimension of about 1 μm. The diffraction image and the Miller indexes (Table 10) confirm that these particles are carbon aggregates. Finally, no metallic particles compounds have been found on the specimen.

Table 10. Test case 15; SAED analysis: nanoparticles diffraction image and experimental diffraction diameters.

	Experimental diameter (A)
	D_1 = 3.37
	D_2 = 2.13
	D_3 = 1.80
	D_4 = 1.21

It can be underlined that, while for rail pressure variations from 50 to 120 bar, increase in concentration of non-carbon nanoparticles have been found on the specimen, in the SOI variations up to 340 CA° there was no evident traces of non-carbon structures, being the copper grids covered only by carbon particles. By coupling the SEM-TEM analyses it is possible to relate the main dimension of soot clusters with the single soot sphere dimension varying the injection strategies. Therefore, Figure 19 and Figure 20 summarize the main dimensions of soot clusters and nanoparticles detected in the above-discussed test cases by means of TEM analyses, highlighting that:

- an increase in rail pressure up to 120 bar leads to an increase in main cluster dimension (about 1.5÷2 µm), while carbon soot nanoparticles diameter remains approximately stable around the value of 38 ± 7 nm;

- an increase in SOI up to 340 CA° bTDC at constant rail pressure of 50 bar leads to an increment of both soot clusters dimension (about 1.5 µm) and carbon nanoparticles main diameter (43 ± 12 nm).

The obtained values for soot dimensions are in good agreement with other researches on GDI emissions [11],[17].
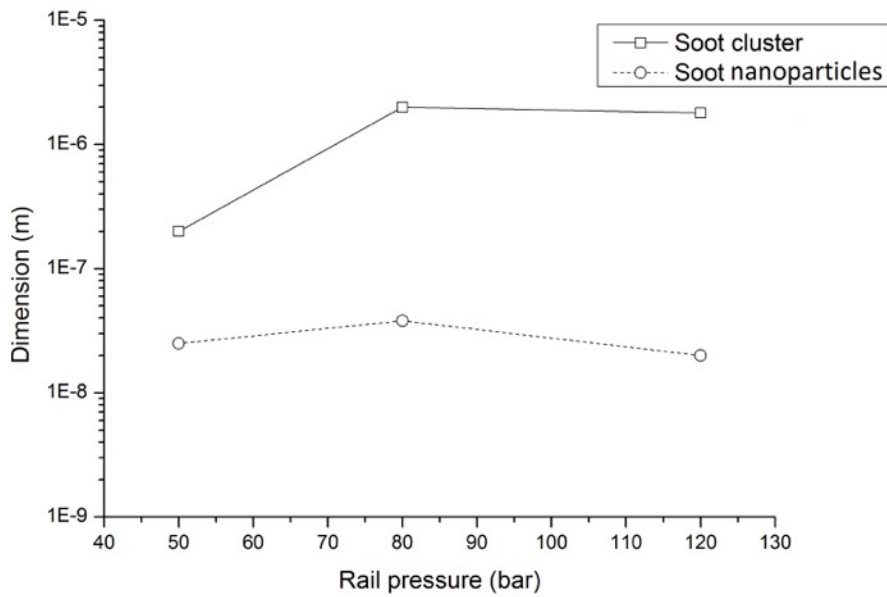
Figure 19. Main dimension of soot clusters and soot nanoparticles as a function of rail pressure at 270 CA°.
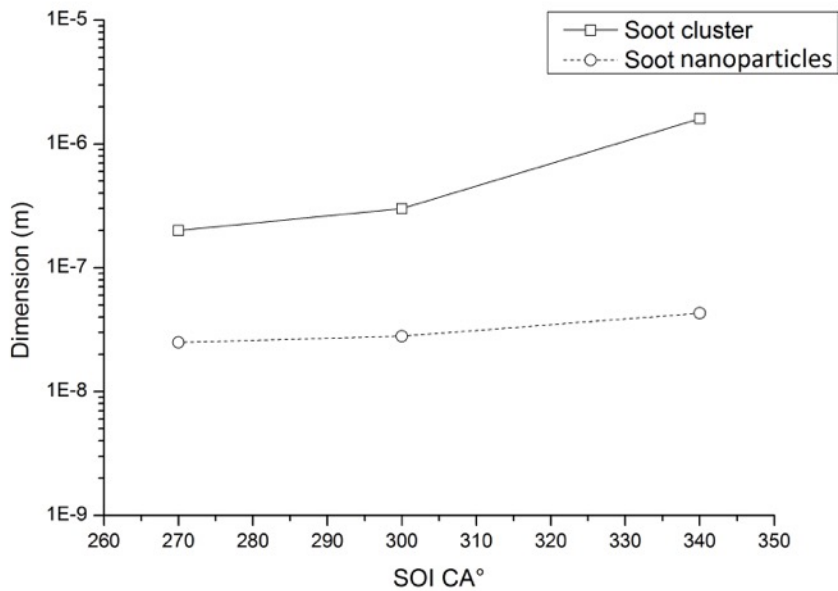

Figure 20. Main dimension of soot clusters and soot nanoparticles as a function of SOI °CA at rail pressure of 50 bar.

In conclusion, after the above-discussed SEM/TEM/SAED /EDX analyses, it can be affirmed that:

- for a rail pressure of 50 bar and 270 CA° SOI, no significant PM/soot formation was detectable on the specimen; an increment in rail pressure up to 80 bar leaded to an increment in soot clusters dimension (about 2 μm with big particles up to 10μm) and quantity; Besides in this condition, soot and metallic particles depositions have been detected. At rail pressure of 120 bar, a further increment in number of soot clusters coupled with a reduction of their mean dimension (down to 1÷2 μm) has been observed: in this case, the metallic particles depositions became relevant, highlighting a strong phenomenon of piston wear;

- starting from 50 bar rail pressure and 270 CA° bTDC SOI, an increase in SOI angle up to 300 CA° bTDC leaded to high sooting conditions; in this case, the clusters were characterized by big particles (dimension about 2÷5 μm) with branched structure and uniformly distributed sub-micron linear dimension structures (about 500 mn). Finally, big soot particles aggregation up to 5 μm have been observed for further SOI increase (340 CA° bTDC).

Moreover, the SOI CA° increase seems to be less harmful for pistons and engine abrasion, since it leads to no formation of metallic compounds at the exhaust but produce higher sooting conditions.

3.2. Continuous gas sampling techniques: Photo Acoustic Detector and DICOM analysis

In the last part of the present study, the relationship between morphology/structure of PM compounds and engine injection strategies has been investigated. Taking into account the results discussed in the previous section, 2 continuous gas sampling techniques, applied by means of 2 different instrumentations (soot concentration by means of AVL MSS and opacity by means of AVL DICOM) have been compared, to provide confirmation about soot/particulate composition.

According to Table 2, all measures of soot concentration and opacity have been performed in 2 different points, before catalyst and at exhaust. Figure 21 and Figure 22 show the soot concentration measurements, carried out by means of AVL MSS, as a function of rail pressure and SOI, respectively.
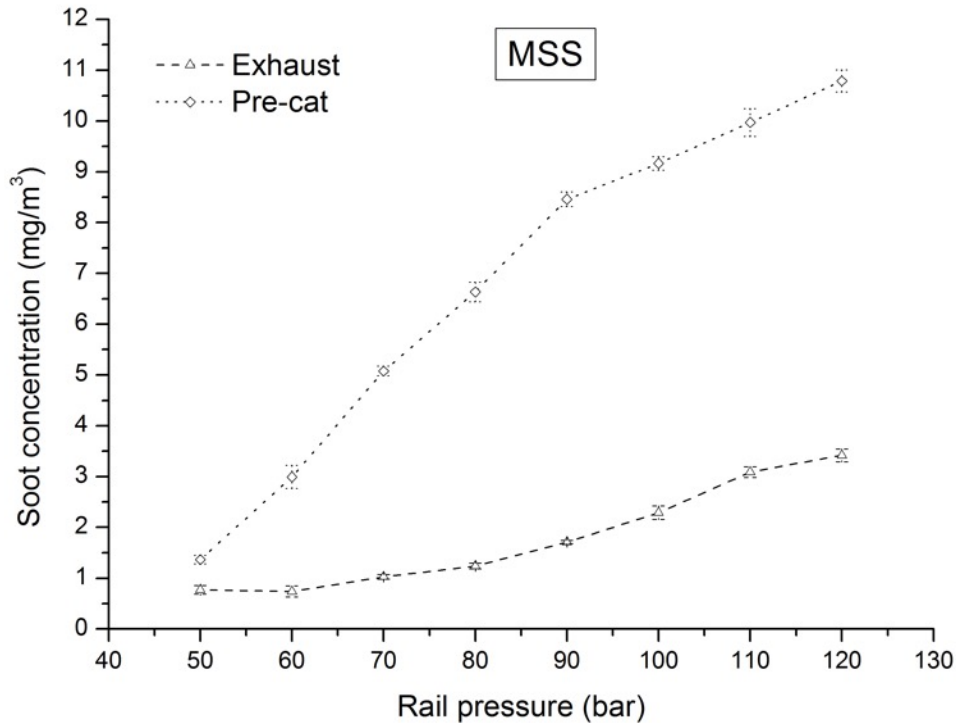
Figure 21. MSS measurements: soot concentration as a function of rail pressure, before catalyst and at exhaust.

By referring to Figure 21, a linear increment in soot production with the rail pressure can be observed before the catalyst. A similar behavior has been found at the exhaust, but with reduced values of soot concentration (about 3 mg/m^3 at 120 bar of rail pressure). As told before, the rail pressure increment leads to formation of non-carbon structures, mainly evident in the 120 bar rail pressure case (Figure 11), and of high dimension carbon particles. As the MSS is able only to detect the carbon component of particulate, low influence of rail pressure variation in emission production was detected at exhaust.
With regards to Figure 22, for low SOI values, the soot concentration increases linearly. Instead, over 300 CA° bTDC a higher increment of soot production in SOI curve can be detected.
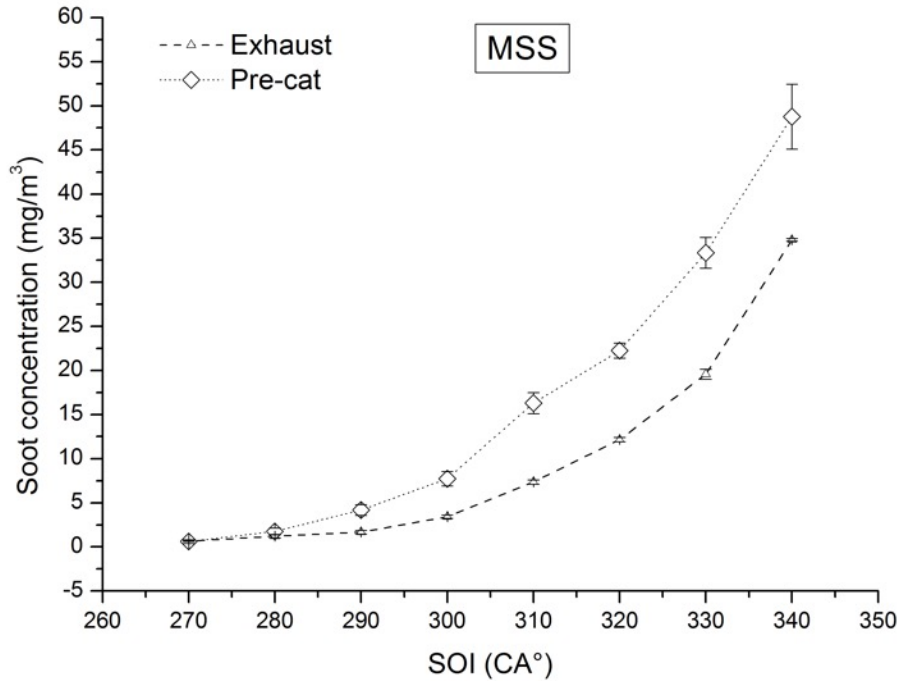
Figure 22. MSS measurements: soot concentration as a function of SOI CA°, before catalyst and at exhaust.

This result can be explained taking into account that from this SOI value there could be a high piston or aspiration valves impingement. Furthermore, it is in accord with the previous TEM analysis: indeed, by referring to Figure 18 at 340 CA° bTDC SOI, the particulate produced by the engine is composed only by carbon particles, that are accurately detected by the MSS. Besides, due to the high quantity of carbon particles, the catalyst is not able to efficiently trap and oxidize the carbonate compound that have been detected also at the exhaust.

In the same operative points, opacimetric measurements, before the catalyst and at the exhaust, have been performed via AVL DICOM 4000 and subsequently compared with MSS and SEM/TEM/SAED/EDX results (Figure 23 and Figure 24).
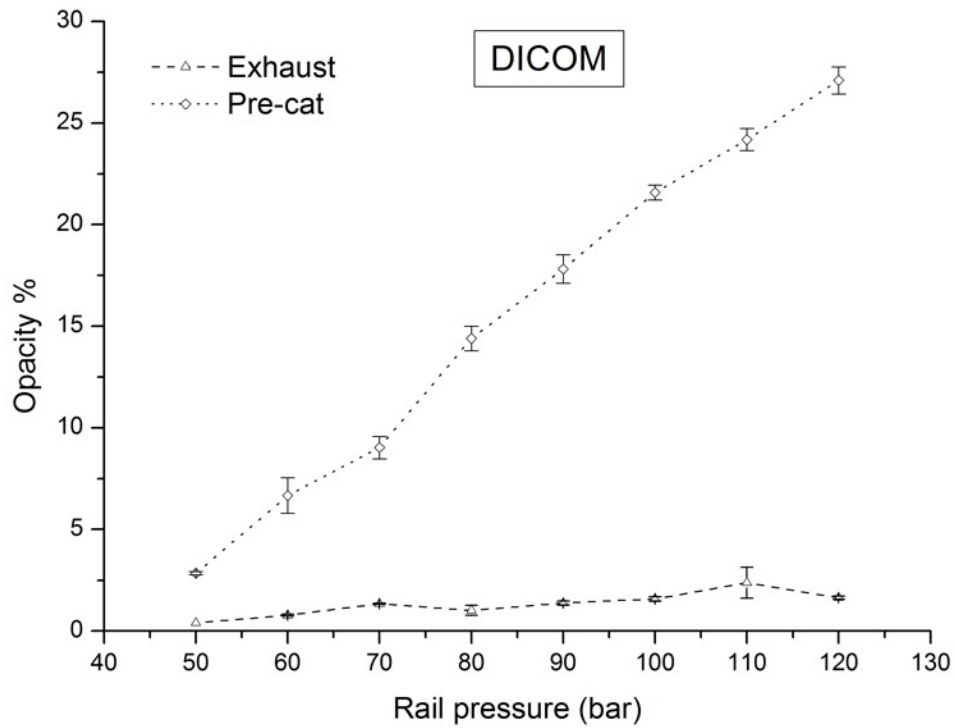
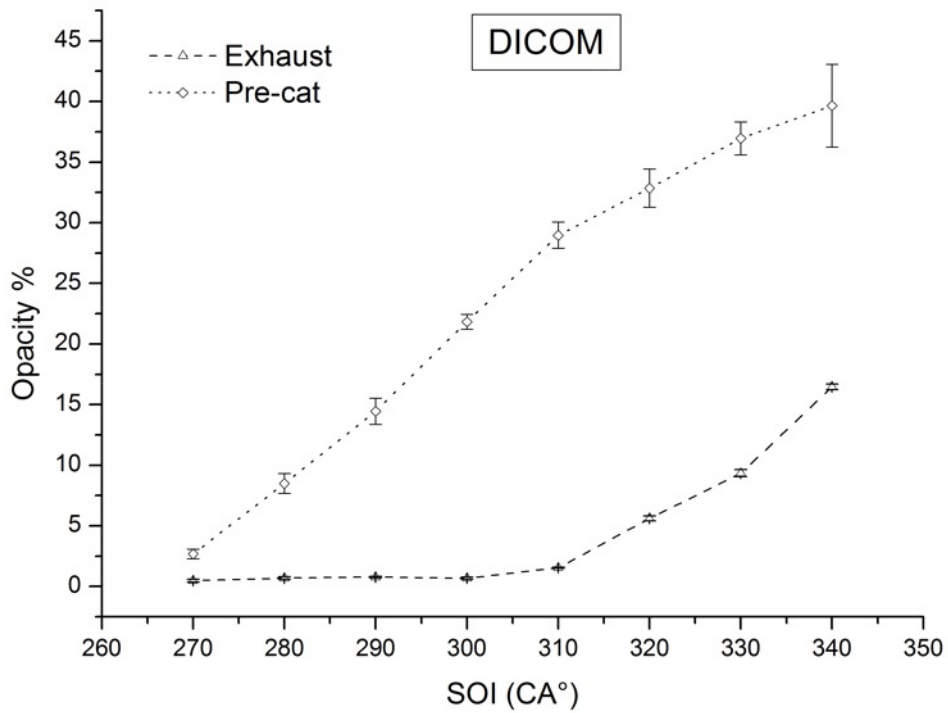Figure 23. Opacity as a function of rail pressure, before catalyst and at exhaust.

Figure 24. Opacity as a function of SOI CA°, before catalyst and at exhaust.

As can be observed, the opacity measured before catalyst increases almost linearly for both rail pressure and SOI increasing, although the influence in absorption coefficient is higher for an injection timing shift toward higher values with respect to rail pressure variation. This result can be explained taking into account that the AVL DICOM 4000 measurements are influenced by all particles producing light absorption, according to Eq. 1. At the exhaust, instead, no influence in emissions quantity has been detected by DICOM for rail pressure variation, while the SOI increment leads to opacity increase with higher values of 310 CA° bTDC. The opacimeter is not able to efficiently detect nanometric particles, as their cross section does not produce a considerable light absorption and, being in the Rayleigh scattering regime, the backscattered component of light (about 50%) produces a reduction of the acquired signal [65],[66].

In conclusion, the above-discussed results allowed to do the following considerations about the catalyst efficiency, expressed as reduction of soot and PM at the engine exhaust:

- even working with different measurement principles and measuring different quantity, a good catalyst efficiency has been measured by AVL MSS and AVL DICOM 400, over all rail pressures under investigation (Figure 21 and Figure 23);

- Figure 22 and Figure 24 demonstrate that catalyst efficiency can reach very good performance (about 90%) for values of SOI up to 300 CA°; over this injection condition, due to the high amount of soot particles, the oxidation reaction into the catalyst is not complete, thus allowing to soot to reach the exhaust.

The actual key point for GDI engines is to reduce production of sub-micrometric particles, since dangerous for human health. As seen from the SEM/TEM analyses and from the MSS/DICOM measurements, injection strategies (variation of rail pressure and SOI) can be considered as key factor to obtain an increase in soot/PM cluster dimension (Figure 19 and Figure 20) , even if total emission amount has to respect the regulation for light duty vehicles. Furthermore, the increase in cluster dimension can improve the gasoline particle filter efficiency, as observed by Viswanathan et al. [70],[71]. Operative points with high clusters dimension (1.5÷2 μm) and reduced amount of soot emission (1.2÷3.5 mg/m^3) can be achieved by rail pressure value higher than 80 bar, although high values of rail pressure should be avoided, leading to relevant piston wear, as observed by means of the TEM analysis at 120 bar.

4. Conclusions

In the present work, several techniques have been used together, to analyze morphology, composition and concentration of particulate matter and soot at the exhaust of a commercial turbocharged, 1.4 litres,

90 kW GDI engine. Particularly, several electronic microscopy images (SEM and TEM) coupled with SAED/EDX analyses have been done. Furthermore, conventional exhaust sampling techniques have been used to measure soot concentration (AVL Micro Soot Sensor) and light absorption due to PM (AVL DICOM 4000). These measurements were carried out at low engine speed (1000 rpm) and loads (50 Nm), by varying rail pressure for gasoline injection (from 50 bar to 120 bar at constant SOI of 270 CA° bTDC) and start of injection before TDC (from 270 to 340 CA° bTDC at constant rail pressure of 50 bar).

The results can be summarized as follows:

- For engine standard conditions of 50 bar and 270 SOI CA°, at exhaust, soot carbon clusters of about 200-500 nm composed by nanoparticles of 25 ± 7 nm have been found. In this case, the soot structure was like a branched cluster. Metallic polycrystalline aggregates of about 600 nm of nano-crystals with mean dimension of 4 ± 1 nm have been detected on the copper grid too. The EDX analysis on these particles revealed that they came from the piston, being compatible with its composition.

- An increase in rail pressure up to 80 bar leaded to an increase in main cluster dimension (about 2 μm) and carbon soot nanoparticles diameter (up to 38 ± 7 nm). The carbon clusters were composed by nanoparticles chains. Besides, higher density and mean dimension (6 ± 1 nm) of metallic nano-crystals have been found. The EDX analysis revealed an increase in non-metallic particles concentration and subsequently a higher piston wear with respect the 50bar, 270 SOI CA° condition.

- At rail pressure of 120 bar, a slight reduction in carbon clusters dimension down to about 1.5 μm has been detected and 3 main soot structures have been found: nano-belts with core-shell morphology, nanotubes and textured nanofoils. All the 3 structures were carbonate compounds, as revealed by the SAED analysis.

- The start of injection up to 300 CA° bTDC at constant rail pressure of 50 bar leaded to an increment of soot with respect to the first operative condition. In this case, the main clusters dimension was about 300 nm, with nanoparticles diameter of 28 ± 5 nm. All detected particles were carbonate aggregates (graphite) as revealed by the diffraction images. No evident presence of metallic particles have been found on the specimen.

- A further increase in SOI up to 340 CA° bTDC leaded to an increment of both soot clusters dimension (about 1.5 μm) and carbon nanoparticles main diameter (43 ± 12 nm). Also in this case only carbonate branched chains have been detected with no metallic polycrystalline presence.

In conclusion, the results clarified the relationship between injection strategies, PM morphology, PM composition and catalyst efficiency:

- increases in rail pressure lead to changes in cluster morphology (from simple nanoparticles chains to nano-belts with core-shell morphology, nanotubes and textured nanofoils), composition (only soot carbon clusters under low pressure condition and traces of metallic polycrystalline aggregates related to the piston wear phenomenon under high pressure condition) and dimension (up to 1.5÷2 μm);
- increases in SOI lead to higher soot production, with negative effects on catalyst efficiency (due to the higher amount of soot particles, the oxidation reaction into the catalyst is not complete, thus allowing to soot to reach the exhaust).

References

[1] J. McCreanor, P. Cullinan, M. J. Nieuwenhuijsen, J. S.-E. E., Malliarou, L. Jarup, R. Harrington, M. Svartengren., I. Han, P. Ohman-Strickland, C. J., Zhang, Respiratory effects of exposure to diesel traffic in persons with asthma, New Eng. J. Med 357 (23) (2007) 2348-2358.

[2] V. Stone, H. Johnston, M. Clift, Air pollution, ultrafine and nanoparticle toxicology: Cellular and molecular interactions, IEEE Transactions on Nanobioscience 6 (4) (2007) 331-340.

[3] H. E. Wichmann, A. Peters, Epidemiological evidence of the effects of ultrafine particle exposure, Philosophical Transactions of the Royal Society of London A: Mathematical, Physical and Engineering Sciences 358 (1775) (2000) 2751-2769.

[4] E. Bardasz, D. Arters, E. Schiferl, D. Righi, A comparison of gasoline direct injection and port fuel injection vehicles: Part II - lubricant oil performance and engine wear, 1999 01 1499.

[5] International Energy Agency, Key world energy statistics 2015.

[6] B.-B. Peng, Y. Fan, J.-H. Xu, Integrated assessment of energy efficiency technologies and CO_2 abatement cost curves in chinas road passenger car sector, Energy Conversion and Management 109 (2016) 195-212.

[7] M. Shahbaz, N. Khraief, M. M. B. Jemaa, On the causal nexus of road transport CO_2 emissions and macroeconomic variables in tunisia: Evidence from combined cointegration tests, Renewable and Sustainable Energy Reviews 51 (2015) 89-100.

[8] P. Leduc, B. Dubar, A. Ranini, G. Monnier, Downsizing of gasoline engine: an efficient way to reduce CO2 emissions, Oil & Gas Science and Technology 58 (1) (2003) 115-127.

[9] C. Silva, M. Ross, T. Farias, Analysis and simulation of low-cost strategies to reduce fuel

consumption and emissions in conventional gasoline light-duty vehicles, Energy Conversion and Management 50 (2009) 215-222.

[10] J. Turner, A. Popplewell, R. PatelT. Johnson, *et al.* Ultra boost for economy: Extending the limits of extreme engine downsizing 1 (2014) 387-417.

[11] A. Liati, D. Schreiber, P. D. Eggenschwiler, Y. A. R. Dasilva, A. C. Spiteri, Electron microscopic characterization of soot particulate matter emitted by modern direct injection gasoline engines, Combustion and Flame 166 (2016) 307-315.

[12] O. A. Kutlar, H. Arslan, A. T. Calik, Methods to improve efficiency of four stroke, spark ignition engines at part load, Energy Conversion and Management 46 (20) (2005) 3202-3220.

[13] D. Fennell, J. Herreros, A. Tsolakis, Improving gasoline direct injection GDI engine efficiency and emissions with hydrogen from exhaust gas fuel reforming, International Journal of Hydrogen Energy 39 (10) (2014) 5153-5162.

[14] Q. Tang, J. Fu, J. Liu, B. Boulet, L. Tan, Z. Zhao, Comparison and analysis of the effects of various improved turbocharging approaches on gasoline engine transient performances, Applied Thermal Engineering 93 (2016) 797-812.

[15] U. Mathis, M. Mohr, A.-M. Forss, Comprehensive particle characterization of modern gasoline and diesel passenger cars at low ambient temperatures, Atmospheric Environment 39 (1) (2005) 107-117.

[16] Y. Luo, L. Zhu, J. Fang, Z. Zhuang, C. Guan, C. Xia, X. Xie, Z. Huang, Size distribution, chemical composition and oxidation reactivity of particulate matter from gasoline direct injection GDI engine fueled with ethanol-gasoline fuel, Applied Thermal Engineering 89 (2015) 647-655.

[17] F. Bonatesta, E. Chiappetta, A. L. Rocca, Part-load particulate matter from a GDI engine and the connection with combustion characteristics, Applied Energy 124 (2014) 366-376.

[18] B. Giechaskiel, M. Maricq, L. Ntziachristos, C. Dardiotis, X. Wang, H. Axmann, A. Bergmann, W. Schindler, Review of motor vehicle particulate emissions sampling and measurement: From smoke and filter mass to particle number, Journal of Aerosol Science 67 (2014) 48-86.

[19] D. B. Kittelson, Engines and nanoparticles: a review, Journal of Aerosol Science 29 (56) (1998) 575-588.

[20] S. Choi, H. Seong, Lube oil-dependent ash chemistry on soot oxidation reactivity in a gasoline direct-injection engine, Combustion and Flame, Volume 174, 2016, Pages 68-76

[21] N. Serhan, A. Tsolakis, F.J. Martos, Effect of propylene glycol ether fuelling on the different physico-chemical properties of the emitted particulate matters: Implications of the soot reactivity,

Fuel, Volume 219, 2018, Pages 1-11

[22] S. Choi, H. Seong, Oxidation characteristics of gasoline direct-injection GDI engine soot: Catalytic effects of ash and modified kinetic correlation, Combustion and Flame 162 (6) (2015) 2371-2389.

[23] M. Sharma, A. K. Agarwal, K. Bharathi, Characterization of exhaust particulates from diesel engine, Atmospheric Environment 39 (17) (2005) 3023-3028.

[24] R. L. V. Wal, A. J. Tomasek, Soot oxidation: dependence upon initial nanostructure, Combustion and Flame 134 (12) (2003) 1-9.

[25] Y. Wei, K. Wang, W. Wang, S. Liu, X. Chen, Y. Yang, S. Bai, Comparison study on the emission characteristics of diesel- and dimethyl ether-originated particulate matters, Applied Energy 130 (2014) 357-369.

[26] Y. Ma, M. Zhu, D. Zhang, Effect of a homogeneous combustion catalyst on the characteristics of diesel soot emitted from a compression ignition engine, Applied Energy 113 (2014) 751-757.

[27] M. Patel, C. L. A. Ricardo, P. Scardi, P. B. Aswath, Morphology, structure and chemistry of extracted diesel soot - Part I: Transmission electron microscopy, Raman spectroscopy, x-ray photoelectron spectroscopy and synchrotron x-ray diffraction study, Tribology International 52 (2012) 29-39.

[28] C. K. Gaddam, R. L. V. Wal, Physical and chemical characterization of SIDI engine particulates, Combustion and Flame 160 (11) (2013) 2517-2528.

[29] L. Chen, Z. Liang, X. Zhang, S. Shuai, Characterizing particulate matter emissions from GDI and PFI vehicles under transient and cold start conditions, Fuel, Volume 189, 2017, Pages 131-140

[30] D. Uy, M. A. Ford, D. T. Jayne, A. E. ONeill, L. P. Haack, J. Hangas, M. J. Jagner, A. Sammut, A. K. Gangopadhyay, Characterization of gasoline soot and comparison to diesel soot: Morphology, chemistry, and wear, Tribology International 80 (2014) 198-209.

[31] D. Lee, S. C. Choi, C. S. Lee, Impact of SME blended fuel combustion on soot morphological characteristics in a diesel engine, International Journal of Automotive Technology 14 (2013) 757 - 762.

[32] Y. An, X. Li, S. Teng, K. Wang, Y. Pei, J. Qin, H. Zhao, Development of a soot particle model with PAHs as precursors through simulations and experiments, Fuel, Volume 179, 2016, Pages 246-257

[33] V. Sharma, D. Uy, A. Gangopadhyay, A. ONeill, W. A. Paxton, A. Sammut, M. A. Ford, P. B. Aswath, Structure and chemistry of crankcase and exhaust soot extracted from diesel engines, Carbon 103 (2016) 327 - 338.

[34] A. Liati, D.l Schreiber, Y. A. R. Dasilva, P. D.Eggenschwiler, Ultrafine particle emissions from

modern Gasoline and Diesel vehicles: An electron microscopic perspective, Environmental Pollution, Volume 239, 2018, Pages 661-669

[35] J. Song, M. Alam, A. L. Boehman, Impact of alternative fuels on soot properties and DPF regeneration, Combustion Science and Technology 179 (9) (2007) 1991-2037.

[36] A. Clague, J. Donnet, T. Wang, J. Peng, A comparison of diesel engine soot with carbon black1, Carbon 37 (10) (1999) 1553-1565.

[37] Y. Jung, C. Bae, Immaturity of soot particles in exhaust gas for low temperature diesel combustion in a direct injection compression ignition engine, Fuel 161 (2015) 312-322.

[38] A. Soewono, S. Rogak, Morphology and raman spectra of engine-emitted particulates, Aerosol Science and Technology 45 (10) (2011) 1206-1216.

[39] O. Can, E. Ozturk, H. Solmaz, F. Aksoy, C. inar, H. S. Yucesu, Combined effects of soybean biodiesel fuel addition and {EGR} application on the combustion and exhaust emissions in a diesel engine, Applied Thermal Engineering 95 (2016) 115-124.

[40] M. Costa, U. Sorge, S. Merola, A. Irimescu, M. L. Villetta, V. Rocco, Split injection in a homogeneous stratified gasoline direct injection engine for high combustion efficiency and low pollutants emission, Energy 117 (2) (2016) 405-415.

[41] S. di Stasio, P. Massoli, Influence of the soot property uncertainties in temperature and volume-fraction measurements by two-colour pyrometry, Measurement Science and Technology 5 (12) (1994) 1453-1465.

[42] F. Naccarato, M. Potenza, A. de Risi, Simultaneous LII and TC optical correction of a low-sooting LPG diffusion flame, Measurement 47 (2014) 989-1000.

[43] B. Menkiel, A. Donkerbroek, R. Uitz, R. Cracknell, L. Ganippa, Measurement of in-cylinder soot particles and their distribution in an optical HSDI diesel engine using time resolved laser induced incandescence (TR-LII), Combustion and Flame 159 (9) (2012) 2985-2998.

[44] C. Leermakers, M. Musculus, In-cylinder soot precursor growth in a low-temperature combustion diesel engine: Laser-induced fluorescence of polycyclic aromatic hydrocarbons, Proceedings of the Combustion Institute 35 (3) (2015) 3079-3086.

[45] F. Catapano, P. Sementa, BM. Vaglieco, Air-fuel mixing and combustion behavior of gasoline-ethanol blends in a GDI wall-guided turbocharged multi-cylinder optical engine, Renewable Energy 96, 319-332, 2016

[46] P. Sementa, BM. Vaglieco, F. Catapano, Thermodynamic and optical characterizations of a high performance GDI engine operating in homogeneous and stratified charge mixture conditions fueled

with gasoline and bio-ethanol, Fuel 96, 204-219, 2012

[47] M. Potenza, F. Naccarato, A. de Risi, Two-dimensional measurements of primary soot diameter in diffusion flames by two-dimensional time resolved laser induced incandescence, IET Science, Measurement & Technology 8 (2014) 107-115(8).

[48] Q. Liu, J. Fu, G. Zhu, Q. Li, J. Liu, X. Duan, Q. Guo, Comparative study on thermodynamics, combustion and emissions of turbocharged gasoline direct injection (GDI) engine under NEDC and steady-state conditions, Energy Conversion and Management, Volume 169, 2018, Pages 111-123

[49] S. Di Iorio, M. Lazzaro, P. Sementa, BM. Vaglieco, F. Catapano, Particle Size Distributions from a DI High Performance SI Engine Fuelled with Gasoline-Ethanol Blended Fuels, SAE Technical Paper 2011-24-0211, 2011

[50] F. Liu, Y. Hua, H. Wu, C.Lee, Z. Wang, Experimental and kinetic investigation on soot formation of n-butanol-gasoline blends in laminar coflow diffusion flames, Fuel, 213 (2018), pages 195-205

[51] B. Lin, H. Gu, B. Guan, D. Han, C. Gu, Z. Huang, H. Lin, Size evolution of soot particles from gasoline and n-heptane/toluene blend in a burner stabilized stagnation flame, Fuel, 203 (2017) pages 135-144

[52] P. Sementa, BM. Vaglieco, F. Catapano, Non-intrusive investigation in a small GDI optical engine fuelled with gasoline and ethanol, SAE International Journal of Engines 4 (1), 50-66, 2011

[53] T. L. Barone, J. M. Storey, A. D. Youngquist, J. P. Szybist, An analysis of direct-injection spark-ignition (disi) soot morphology, Atmospheric Environment 49 (2012) 268-274.

[54] C. Hergueta, M. Bogarra, A. Tsolakis, K. Essa, J.M. Herreros, Butanol-gasoline blend and exhaust gas recirculation, impact on GDI engine emissions, Fuel, Volume 208, 2017, Pages 662-672

[55] J. M. Christensen, J.-D. Grunwaldt, A. D. Jensen, Importance of the oxygen bond strength for catalytic activity in soot oxidation, Applied Catalysis B: Environmental 188 (2016) 235-244.

[56] D. Fino, S. Bensaid, M. Piumetti, N. Russo, A review on the catalytic combustion of soot in diesel particulate filters for automotive applications: From powder catalysts to structured reactors, Applied Catalysis A: General 509 (2016) 75–96.

[57] W. de Ruijter, R. Sharma, M. McCartney, D. J. Smith, Measurement of lattice-fringe vectors from digital images: experimental precision, Ultramicroscopy 57 (4) (1995) 409-422.

[58] C. Zhang, Q. Yao, J. Sun, Characteristics of particulate matter from emissions of four typical coal-fired power plants in china, Fuel Processing Technology 86 (7) (2005) 757-768.

[59] W. Shangguan, Y. Teraoka, S. Kagawa, Kinetics of soot-O_2, soot-NO and soot-O_2-NO reactions over spinel-type $CuFe_2O_4$ catalyst, Applied Catalysis B: Environmental 12 (23) (1997) 237-247.

[60] R. Dobbins, C. Megaridis, Morphology of flame-generated soot as determined by thermophoretic sampling., Langmuir 3 (2) (1987) 254-259.

[61] D. Zhang, Y. Ma, M. Zhu, Nanostructure and oxidative properties of soot from a compression ignition engine: The effect of a homogeneous combustion catalyst, Proceedings of the Combustion Institute 34 (1) (2013) 1869-1876.

[62] U. O. Koylu, C. McEnally, D. Rosner, L. Pfefferle, Simultaneous measurements of soot volume fraction and particle size microstructure in flames using a thermophoretic sampling technique, Combustion and Flame 110 (4) (1997) 494-507.

[63] A. Petzold, R. Niessner, Photoacoustic soot sensor for in-situ black carbon monitoring, Applied Physics B 63 (2) (1996) 191-197.

[64] I. Koichi, Powder and Bulk Solids Handling Processes: Instrumentation and Control, Hoepli, 1988.

[65] H. Hottel, A. Sarofim, Radiative Transfer, McGraw-Hill series in mechanical engineering, McGraw-Hill, 1967.

[66] C. F. Bohren, D. R. Huffman, Absorption and Scattering of Light by Small Particles, Wiley-VCH, 1998.

[67] J. W. Edington, Practical electron microscopy in materials science, N.V. Philips in Eindhoven, 1976.

[68] A. Bescond, J. Yon, F. X. Ouf, D. Ferry, D. Delhaye, D. Gaffié, A. Coppalle & C. Rozé (2014) Automated Determination of Aggregate Primary Particle Size Distribution by TEM Image Analysis: Application to Soot, Aerosol Science and Technology, 48:8, 831-841.

[69] M. A. Asadabad, M. J. Eskandari, Modern electron microscopy in physical and life sciences. InTech, 2016.

[70] S.Viswanathan, D.Rothamer, A.Zelenyuk, M.Stewart, D.Bell, Experimental investigation of the effect of inlet particle properties on the capture efficiency in an exhaust particulate filter, Journal of Aerosol Science 113 (2017) 250-264

[71] J. Yang, M. Stewart, G. Maupin, D. Herling, A. Zelenyuk, Single wall diesel particulate filter (DPF) filtration efficiency studies using laboratory generated particles, Chemical Engineering Science, 64 (2009), 1625-1634